

The search for active black holes in nearby low-mass galaxies using optical and mid-IR data

Lia F. Sartori^{1*}, Kevin Schawinski¹, Ezequiel Treister², Benny Trakhtenbrot^{1,†},
Michael Koss^{1,‡}, Maryam Shirazi¹, Kyuseok Oh^{1,3}

¹*Institute for Astronomy, Department of Physics, ETH Zürich, Wolfgang-Pauli-Strasse 27, CH-8093 Zürich, Switzerland*

²*Universidad de Concepción, Departamento de Astronomía, Casilla 160-C, Concepción, Chile*

³*Department of Astronomy, Yonsei University, Seoul 120-749, Republic of Korea*

[†]*Zwicky Fellow*

[‡]*Ambizione Fellow*

27 September 2018

ABSTRACT

We investigated AGN activity in low-mass galaxies, an important regime that can shed light onto BH formation and evolution, and their interaction with their host galaxies. We identified 336 AGN candidates from a parent sample of $\sim 48,000$ nearby low-mass galaxies ($M_* \leq 10^{9.5} M_\odot$, $z < 0.1$) in the SDSS. We selected the AGN using the classical BPT diagram, a similar optical emission line diagnostic based on the He II $\lambda 4686$ line, and mid-IR color cuts. Different criteria select host galaxies with different physical properties such as stellar mass and optical color and only 3 out of 336 sources fulfill all three criteria. This could be in part due to selection biases. The resulting AGN fraction of $\sim 0.7\%$ is at least one order of magnitude below the one estimated for more massive galaxies. At optical wavelengths, the He II-based AGN selection appears to be more sensitive to AGN hosted in star-forming galaxies than the classical BPT diagram, at least in the low-mass regime. The archival X-ray and radio data available for some of the optically selected AGN candidates seem to confirm their AGN nature, but follow-up observations are needed to confirm the AGN nature of the rest of the sample, especially in the case of mid-IR selection. Our sample will be important for future follow-up studies aiming to understand the relation between BHs and host galaxies in the low-mass regime.

Key words: galaxies: active – galaxies: dwarf – galaxies: nuclei – galaxies: Seyfert – infrared: galaxies

1 INTRODUCTION

The formation of Supermassive Black Holes (SMBHs) and their interplay with their host galaxies are fundamental issues in the study of galaxy formation and evolution. Different studies showed that SMBHs with masses $M_{\text{BH}} \sim 10^6 - 10^9 M_\odot$ reside in most of the massive galaxies (stellar mass $M_* \gtrsim 10^{10} M_\odot$) in the present-day universe, including the Milky Way (e.g. Kormendy & Richstone 1995; Schödel et al. 2003; Kormendy & Ho 2013). Moreover, SMBHs are thought to grow and evolve in a coordinated manner with the galaxies in which they reside. This idea is supported by the observation of massive galaxies where the SMBH mass is correlated to different

host galaxy properties such as stellar mass (Marconi & Hunt 2003), luminosity (e.g. Bentz et al. 2009; Gültekin 2009), and velocity dispersion (e.g. Ferrarese & Merritt 2000; Gebhardt et al. 2000; Tremaine et al. 2002; Gültekin 2009) of the bulge.

The current observational capabilities do not allow us to directly observe seed BHs and their host galaxies in the early universe. However, dwarf galaxies ($M_* \lesssim 10^{9.5} M_\odot$) are supposed to be similar to the precursors of today’s large galaxies and host BHs with masses similar to the first seed BHs (Bellovary et al. 2011). The study of dwarf galaxies hosting massive BHs can thus provide important information about SMBH formation and evolution, as well as their interaction with their host galaxies. In addition, the present epoch ($z \sim 0$) BH occupation fraction

* E-mail: lia.sartori@phys.ethz.ch

and mass distribution of low-mass galaxies may help in discriminating between different BH formation scenarios, as discussed by Volonteri, Lodato & Natarajan (2008). In fact, although the numbers are still highly uncertain, different BH formation mechanisms at high redshift predict BH seeds with different properties and evolution, and this will result in a different fraction of galaxies containing SMBHs at later times. The two widely discussed scenarios are heavy seeds from the direct collapse of metal-free gas clouds in the early Universe (e.g. Haehnelt & Rees 1993; Lodato & Natarajan 2006; Begelman, Volonteri & Rees 2006), and light seeds from the death of massive first generation (Pop III) stars (e.g. Bromm, Coppi & Larson 1999, Bromm & Yoshida 2011).

One of the most reliable ways to detect a SMBH and to infer its mass is through the analysis of stellar and/or gas dynamics in the host galaxy. However, the gravitational sphere of influence of low-mass BHs in dwarf galaxies is too small to be resolved beyond the Local Group (see Reines, Greene & Geha 2013 for more details). This means that BHs with $M_{\text{BH}} \sim 10^5 - 10^6 M_{\odot}$ outside the Local Group can currently be detected only if they are accreting, i.e. if the galaxy hosts an Active Galactic Nucleus (AGN).

In the last years, two studies have searched for AGN in low-mass galaxies in the Sloan Digital Sky Survey (*SDSS*). Reines, Greene & Geha (2013) searched for optical signatures of accreting BHs in a sample of $\sim 25,000$ nearby low-mass galaxies ($z < 0.055$, $M_{\star} < 3 \times 10^9 M_{\odot}$) selected from the NASA-Sloan Atlas. Applying standard BPT diagram they found an AGN fraction of $\sim 0.13\%$ ¹. Moran et al. (2014) identified 28 AGN out of a sample of $\sim 7,500$ objects in the *SDSS* ($0.003 < z < 0.0177$, AGN host galaxies with $M_{\star} < 10^{10} M_{\odot}$). They derived a lower limit on the AGN fraction of a few percent, but considering a different parent sample than in Reines, Greene & Geha (2013). A different approach was proposed by Satyapal et al. (2014), who applied mid-IR selection techniques to search for AGN in a sample of bulgeless galaxies. They found that mid-IR selection identifies a different AGN population compared to optical selection, and that the fraction of mid-IR selected AGN is higher at lower masses. In a recent study, Marleau et al. (2014) assembled a sample of 313 nearby dwarf galaxies that display mid-IR signature of BH activity. They examined the $M_{\star} - M_{\text{BH}}$ relationship and found that this relation extends also in the low-mass regime (stellar mass in the range $10^5 - 10^9 M_{\odot}$, BH mass in the range $10^2 - 10^6 M_{\odot}$). The literature also offers other studies which attempt to search for low-mass BHs using mid-IR observations (e.g. Satyapal et al. 2007, 2008, 2009; Goulding et al. 2010) or X-ray observations (Ghosh et al. 2008; Desroches & Ho 2009; Gallo et al. 2008, 2010; Kamizasa, Terashima & Awaki 2012; Miller et al. 2012; Schramm et al. 2013). Studies aiming to search for AGN with low-mass BHs using optical data were presented by Greene & Ho (2004, 2007) and Dong et al. (2012). However, most of these works covered only small volumes with mixed

selection functions, and the true BH occupation fraction is poorly understood.

In this work, we combine optical emission line and mid-IR data to search for AGN in nearby low-mass galaxies ($z < 0.1$, $M_{\star} < 10^{9.5} M_{\odot}$), and analyse the properties of their host galaxies. We chose these thresholds for M_{\star} and z because: 1) the difference in the present epoch occupation fraction due to the different formation scenarios is more evident for low-mass galaxies, especially in the mass range $10^{8.5} M_{\odot} < M_{\star} < 10^{9.5} M_{\odot}$ (Greene 2012, based on models of Volonteri, Lodato & Natarajan 2008), and 2) dwarf galaxies are faint and can be observed only in the nearby universe. In this way we measure the fraction of dwarf galaxies containing AGN, placing a lower limit for the BH occupation fraction. Further, assembling a sample of low-mass galaxies hosting AGN is an important step in understanding the relation between BH and host galaxy in the low-mass regime. Because of different biases, the comparison of different selection techniques allows us to find a more complete AGN sample.

The sample selection is described in Section 2. Sections 3 – 5 describe the analysis techniques performed. The discussion of the results and the summary are found in Sections 6 and 7. Finally, an overview of the AGN candidate samples and of the host galaxy properties is given in the Appendix.

2 SAMPLE SELECTION

2.1 Parent sample of nearby dwarf galaxies

We assembled a sample of nearby dwarf galaxies in the *SDSS* DR7 (Abazajian et al. 2009) starting from the *OSSY* catalog (*Oh - Sarzi - Schawinski - Yi*, Oh et al. 2011). The *OSSY* catalog provides line measurements for the entire spectral atlas from *SDSS* DR7 with redshift $z < 0.2$, as well as fitting quality assessment parameters². We selected the objects in the catalog with *SDSS* SpecClass = 2 (galaxy) and redshift lower than $z = 0.1$. We then matched the sample to the MPA-JHU catalog (Kauffmann et al. 2003b; Brinchmann et al. 2004) to obtain the stellar mass, and selected the galaxies with mass lower than $M_{\star} = 10^{9.5} M_{\odot}$. These masses were derived using fits to photometry and assuming $h = 0.7$. We further excluded 0.17% of the objects because of unreliable mass estimation. The final sample of nearby dwarf galaxies consists on 48,416 objects.

Fig. 1 shows the absolute *r*-band magnitude versus redshift distribution of the nearby dwarf galaxy sample. About 15% of the sample is fainter than the *SDSS* spectroscopic apparent magnitude limit $r = 17.77$ mag (petrosian magnitude). Objects below the spectroscopic limit were often targeted in *SDSS* as quasars (e.g. QSO_CAP, QSO_SKIRT target), but successively classified as galaxies (SpecClass = 2), so we kept them into the initial parent sample. However, we did not consider objects with $r > 17.77$ mag for the study of the AGN fraction in dwarf galaxies (Section 3) and of the host galaxy properties (Section 4).

¹ Reines, Greene & Geha (2013) considered in their analysis both Seyfert (35) and composite (101) objects. The fraction we cite corresponds only to the objects classified as Seyferts.

² The object IDs used in this work refer to the source sequence numbers as they appear in the *OSSY* database.

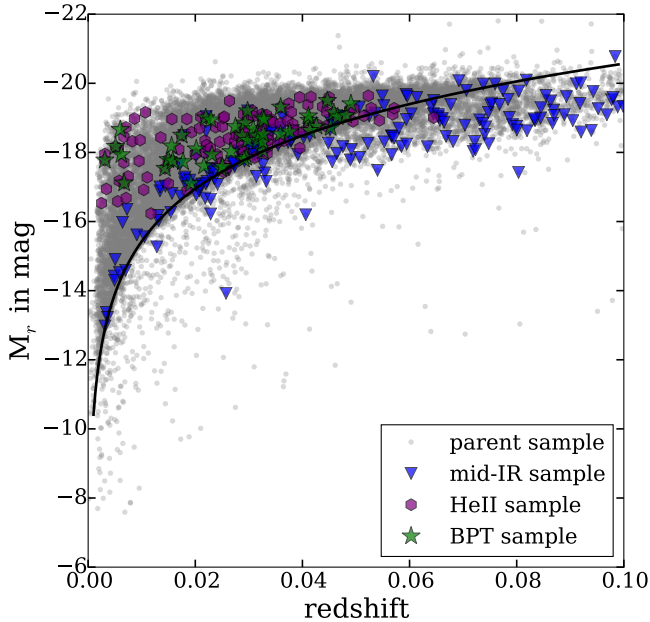


Figure 1. Absolute r -band magnitude (petrosian) versus redshift for the total sample (gray points) and AGN candidates selected with different selection techniques (see Section 2.2). The black solid line corresponds to the *SDSS* spectroscopic apparent magnitude limit, $r = 17.77$ mag. About 15% of the sample lies below this line and will not be considered for the study of the AGN fraction in dwarf galaxies and of the host galaxy properties.

2.2 Selection of AGN candidates

We searched for AGN in the nearby dwarf galaxy sample by applying three AGN selection techniques, which we discuss in detail in what follows:

- 1) classical BPT selection (optical emission line diagnostic) based on the separation lines defined by Kewley et al. (2001), Kauffmann et al. (2003a) and Schawinski et al. (2007);
- 2) the emission line diagnostic based on He II $\lambda 4686$ described by Shirazi & Brinchmann (2012) (in the following *Shirazi He II diagram*); and
- 3) the mid-IR color criteria described by Stern et al. (2012) and Jarrett et al. (2011).

In order to define a clean sample of AGN we corrected the obtained sample for fragmentation. In fact, the *SDSS* catalog is contaminated by many fragmented pieces of extended massive galaxies, which can be erroneously selected as dwarf galaxies. The number of fragmented galaxies in the parent sample should be low enough to not influence the study of the AGN fraction in dwarf galaxies. However, fragmented galaxies have to be removed from the selected AGN sample. In order to find these objects we performed two tests. First, we compared the stellar mass given in *MPA-JHU* with the measurements reported in the *NASA-Sloan Atlas*³ (*NSA*). Because of the definition of the *NSA* catalog this was possible only for galaxies with redshift $z < 0.055$. We then visually inspected the optical images provided by *SDSS*.

³ <http://www.nsatlas.org>

In this way we excluded 33 objects. The list of the AGN candidates is given in Appendix A.

2.2.1 BPT selection

Emission line ratios allow to classify line-emitting galaxies based on their main source of ionization and excitation. The standard diagnostic diagram (Baldwin, Phillips & Terlevich 1981, *BPT diagram*; Veilleux & Osterbrock 1987; Terlevich et al. 1991; Kewley et al. 2001; Kauffmann et al. 2003a; Stasińska et al. 2006; Schawinski et al. 2007) uses $[\text{O III}]\lambda 5007\text{\AA}/\text{H}\beta$ versus $[\text{N II}]\lambda 6583\text{\AA}/\text{H}\alpha$. On this plot, star-forming galaxies lie below the so-called maximum starburst line (Kewley et al. 2001) and form a sequence from low metallicity (low $[\text{N II}]/\text{H}\alpha$, high $[\text{O III}]/\text{H}\beta$) to high metallicity (high $[\text{N II}]/\text{H}\alpha$, low $[\text{O III}]/\text{H}\beta$). Beyond the maximum starburst line the dominant source of ionization is due to mechanisms other than star formation, such as BH accretion, shocks or evolved stellar populations. The objects residing in this region can be divided into Seyfert galaxies (high ionization emission) and Low Ionization Emission Region galaxies (LINERs, Heckman 1980), as proposed by Schawinski et al. (2007) (see also Ho 2008 and references therein). Because of the different ratio of ionisation emission, in fact, Seyfert galaxies and LINERs show different emission line ratios, and are found in different regions of the diagnostic diagram. While Seyfert emission is primarily driven by AGN, LINERs can be powered also by fast shocks (Heckman 1980; Dopita & Sutherland 1995), photoionization by old, metal-rich stellar population (Alonso-Herrero et al. 2000; Taniguchi, Shioya & Murayama 2000; Sarzi et al. 2010), or photoionization by hot stars (Filippenko & Terlevich 1992; Shields 1992; Maoz et al. 1998; Barth & Shields 2000). In our study we consider only Seyfert galaxies as AGN candidates. A further demarcation line, the so-called pure starburst line (Kauffmann et al. 2003a), divides pure star-forming galaxies and AGN from composite galaxies, where the ionizing radiation of AGN and star formation is comparable (Panessa et al. 2005; Kewley et al. 2006; Trouille, Barger & Tremonti 2011).

Emission line diagnostics are significantly affected by biases which can cause a significant fraction of AGN in dwarf galaxies to be missed. Low-metallicity AGN have lower $[\text{N II}]/\text{H}\alpha$ ratios and smaller spread in $[\text{O III}]/\text{H}\beta$ (Kewley et al. 2013; Groves, Heckman & Kauffmann 2006; Ludwig et al. 2012) and they move to the left part of the BPT diagram, often overlapping with the star-forming region. Kewley et al. (2013) claimed that AGN are difficult to distinguish from pure star-forming galaxies using the $[\text{N II}]/\text{H}\alpha$ BPT diagram for metallicities lower than $\log(O/H) + 12 \sim 8.4$. Furthermore, BPT selection is not sensitive to blue galaxies with ongoing star formation, which dilutes the signatures of BH accretion. This is an important issue for dwarf galaxies, as they are smaller in the sky and a big fraction of their light falls within the *SDSS* fiber ($r = 1.5$ arcseconds). The detected emission can therefore be dominated by galaxy light from ongoing star formation, dust and gas, so the optical signatures of BH accretion can no longer be detected (Moran, Filippenko & Chornock 2002).

We identified a sample of AGN candidates using the standard BPT diagram, starting from the observed emission line fluxes given in the *OSSY* catalog. We decided to perform the BPT selection using the $[\text{O III}]/\text{H}\beta$ versus $[\text{N II}]/\text{H}\alpha$ diagnostic diagram since $[\text{N II}]$ is the best indicator for low-metallicity AGN, and dwarf galaxies are expected to have low metallicities (e.g. Groves, Heckman & Kauffmann 2006). For this analysis we required all the lines used for the BPT selection to be detected, and amplitude to noise $\text{AON} > 3$ for $\text{H}\alpha$, $[\text{O III}]$ and $[\text{N II}]$. In the cases where only $\text{H}\beta$ does not fulfill the requirement $\text{AON} > 3$, we estimated the upper limit of the flux from the standard deviation of the *SDSS* spectrum around the line, and assuming the same σ value given for the $[\text{O III}]$ line (σ_{Balmer} in *OSSY*). This gives a lower limit for $[\text{O III}]\lambda 5007\text{\AA}/\text{H}\beta$.

The results are shown in Fig. 2 (left panel). There are 48 galaxies in the Seyfert region of the BPT diagram (in the following we refer to these galaxies as *BPT selected AGN candidates*). Out of the 48 AGN candidates, 40 have $\text{AON} > 3$ in all the lines, while 8 have upper limits for the $\text{H}\beta$ flux⁴. Even with the inclusion of these less reliable candidates, only $\sim 0.1\%$ of the galaxies in the parent sample can be considered as AGN candidate by analysing these specific optical emission line ratios ($\sim 0.08\%$ if we consider only objects with $\text{AON} > 3$ in each line).

2.2.2 He II $\lambda 4686$

As explained above, the classical BPT selection is not very sensitive at low metallicities and for faint AGN, as well as for galaxies with strong ongoing star formation. This can be improved by using lines originating from the mostly neutral interstellar medium, as for example He II $\lambda 4686$ (e.g. Shirazi & Brinchmann 2012). Because of the high ionization energy of He^+ , $E_{\text{ion}} = 54.4$ eV (as a comparison, the ionization potential of O^{++} is 35.5 eV), the He II $\lambda 4686\text{\AA}$ emission line can be produced only in the presence of sources of hard ionization radiation. Therefore, the detection of a luminous He II emission line is a strong indication of AGN activity.

We plotted the He II $\lambda 4686\text{\AA}/\text{H}\beta$ line ratio versus $[\text{N II}]\lambda 6583\text{\AA}/\text{H}\alpha$ diagram described in Shirazi & Brinchmann (2012), and used it as an alternative emission lines diagnostic. Similar to the standard BPT diagram, star-forming galaxies are expected to be below a maximum starburst line, while AGN⁵ are found above this line. We required an amplitude to noise $\text{AON} > 3$ for HeII, $[\text{N II}]$, $\text{H}\beta$ and $\text{H}\alpha$. With this technique selected 121 AGN candidates, as shown in Fig. 3 (middle panel), which correspond to $\sim 0.25\%$ of the parent sample. In the following we refer to these galaxies as He II *selected AGN candidates*.

⁴ We computed the upper limits for $\text{H}\beta$ as 5 times the noise in the spectrum. This corresponds approximately to a detection with signal-to-noise $S/N = 3$. However the number of AGN selected with $\text{H}\beta$ upper limits strongly depends on the upper limits estimation. For example, considering the upper limit as 3 times the noise allow to select 25 additional objects.

⁵ No distinction is made here between Seyferts and LINERs.

2.2.3 Mid-IR color selection

Mid-IR selection relies on the fact that AGN show redder mid-IR colors compared to star-forming galaxies, especially at low redshift (Stern et al. 2012; Assef et al. 2012). The hot dust surrounding the AGN produces a strong mid-IR continuum which can be approximated as a power-law dominating in the redder part of the spectrum. On the other hand, the stellar emission is dominated by a composite black body curve which peaks at rest frame $\sim 1.6\mu\text{m}$. An advantage of mid-IR selection compared to selections based on other wavelength ranges is that mid-IR emission is independent of the viewing angle. This allows to select both unobscured (Type 1) and obscured (Type 2) AGN.

Several mid-IR diagnostic diagrams have been proposed and employed in the literature (e.g. Lacy et al. 2004; Assef et al. 2010; Stern et al. 2005, 2012; Jarrett et al. 2011). In this work we concentrate on cuts which purely rely on the *WISE* bands at 3.4, 4.6, 12 and 22 μm (*W1*, *W2*, *W3* and *W4* bands, respectively; Wright et al. 2010). Stern et al. (2012) proposed a cut based on the *W1* and *W2* bands, the two bluest, most sensitive channels. Using IRAC-selected AGN as their input sample (Stern et al. 2005) they empirically defined a simple color criterion:

$$[W1 - W1] \geq 0.8.$$

For this criterion they estimated a reliability of 95%. A more restrictive criterion was defined by Jarrett et al. (2011), which also considers the *W3* band:

$$2.2 < [W2 - W3] < 4.2$$

$$(0.1 \times [W2 - W3] + 0.38) < [W1 - W2] < 1.7.$$

Even though mid-IR selection is sensitive to both obscured and unobscured AGN, none of the proposed cuts can provide a complete sample of AGN. For less powerful AGN the dilution by the host galaxy may cause a bluer (*W1 - W2*) color, so that these AGN are no longer distinguishable from normal galaxies.

We performed mid-IR color selection following the color cuts described by Stern et al. (2012) and Jarrett et al. (2011). For this we used the *WISE* magnitudes measured with profile-fitting photometry as listed in the *WISE All-Sky Data Release* (Cutri & et al. 2012). For the Stern selection we required the objects to be detected in the *W1* and *W2* bands (in the *WISE* catalog this means $S/N > 2$). For the Jarrett cut we additionally required the detection in the *W3* band. The results are shown in Fig. 4 (right panel). Combining the objects selected by the Stern and Jarrett criteria we found 189 mid-IR candidates. Therefore, $\sim 0.4\%$ of the parent sample exhibits mid-IR colors consistent with AGN emission. In the following analysis we will refer to the objects selected with Stern and/or Jarrett criteria as *mid-IR selected AGN candidates*.

We decided to use the magnitudes measured with profile-fitting photometry in order to be consistent with Stern et al. (2012), but it is important to notice that these magnitudes could be wrong for some extended nearby galaxy. Among the 189 mid-IR selected AGN candidates only 1 is flagged as possibly extended. However, we examined the *WISE* images by eye and the extension in *W1*,

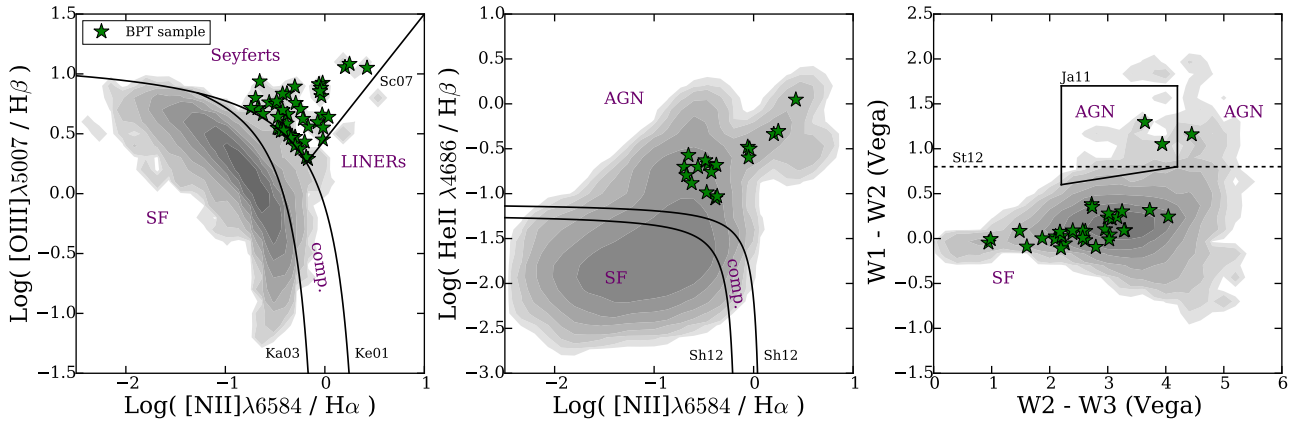


Figure 2. Position of the BPT selected AGN candidates on the three selection diagrams applied in this study. The green stars correspond to the BPT selected AGN candidates (48 objects on the BPT diagram), while the gray shaded areas show the position of the objects in the parent sample of nearby dwarf galaxies. On each plot, only the objects which fulfill our AON or SN cuts (see Section 2.2 for more details) are plotted. *Left:* BPT diagram based on the separation lines defined by Kewley et al. (2001, maximum starburst line), Kauffmann et al. (2003a, pure starburst line) and Schawinski et al. (2007, Seyferts-LINERs separation line). *Middle:* He II emission lines diagram as described in Shirazi & Brinchmann (2012). All the BPT selected AGN candidates with well detected He II emission lines are selected as AGN also with this diagram. *Right:* Mid-IR color-color diagram based on *WISE* colors. The straight and solid lines show the selection cuts described by Stern et al. (2012) and Jarrett et al. (2011), respectively. Only 3 BPT selected AGN candidates are selected as AGN also by applying mid-IR color cuts.

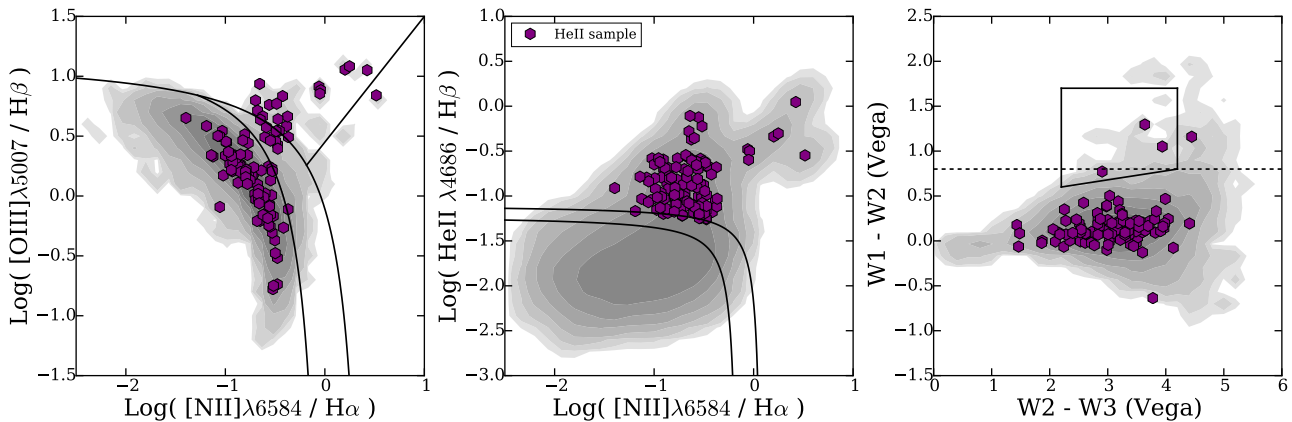


Figure 3. Same as Fig. 2 but for He II selected AGN candidates (purple hexagons). *Left:* BPT diagram. 18 He II selected AGN candidates are selected as Seyfert galaxies in the BPT diagram. *Middle:* Shirazi He II diagram. All the objects found above the pure starburst line described in Shirazi & Brinchmann (2012) are selected as AGN (121 objects). *Right:* Mid-IR color-color diagram. Only 4 of the He II selected AGN candidates are selected as AGN also by applying mid-IR selection.

$W2$ and $W3$ is minimal, so that it will not affect the result significantly.

The *SDSS* spectra of some mid-IR selected AGN required further fitting. For these objects we performed our own fits and computed the observed flux for He II $\lambda 4686$, $H\beta$, $[O III]\lambda 4959$, $[O III]\lambda 5007$, $H\alpha$, $[N II]\lambda 6548$ and $[N II]\lambda 6583$. We fitted the lines with a Gaussian profile, using a fixed ratio between the two $[O III]$ lines and between the two $[N II]$ lines.

2.2.4 Comparison between the selection techniques

The different selection techniques revealed different samples of AGN candidates. In Fig. 2, 3 and 4 we overplotted the AGN candidates selected with each selection technique on the other diagnostic diagrams.

Among 48 BPT selected AGN candidates (Fig. 2), only 3 present mid-IR colors attributable to AGN activity. On the other hand, all the BPT selected AGN candidates with well detected He II emission lines are selected as AGN also by the He II criterium.

In a similar manner, only 4 of the He II selected AGN candidates (Fig. 3) are selected as AGN also by applying mid-IR selection. On the BPT diagram, 18 He II selected AGN candidates are found in the Seyfert region. Here it is important to notice that the requirement $AON > 3$ for the He II line is fulfilled only for 1.7% of the objects in the parent sample of nearby dwarf galaxies. On the other hand, 37.5% of the BPT selected AGN candidates and 21.9% of the mid-IR selected AGN candidates show strong He II emission lines.

Consistently with what described above, most of the

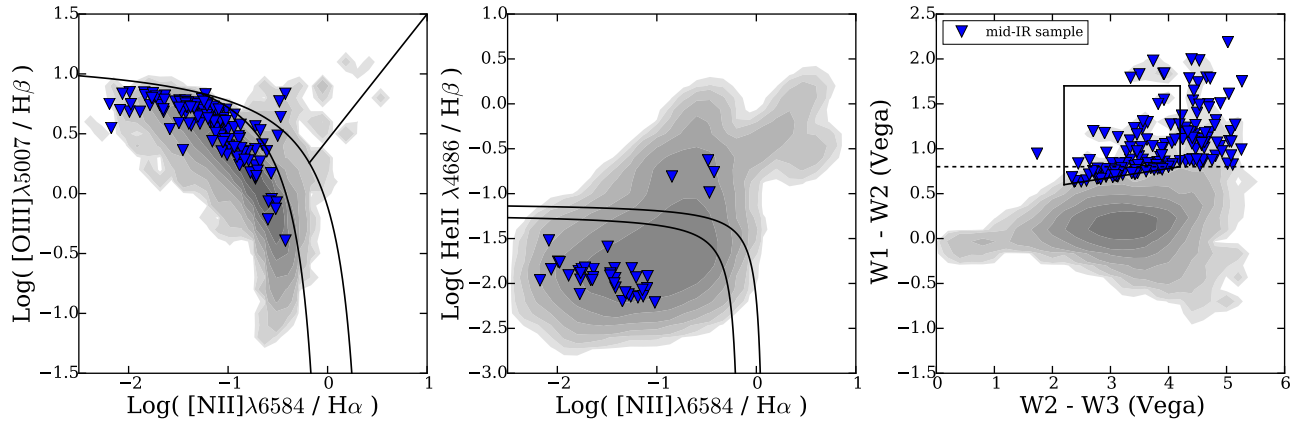


Figure 4. Same as Fig. 2 but for mid-IR selected AGN candidates (blue triangles). *Left:* BPT diagram. Most of the mid-IR selected AGN candidates are located in the upper part of the star-forming region, near to the demarcation line. *Middle:* Shirazi He II diagram. Only 4 mid-IR selected AGN candidates reside on the AGN region of the Shirazi He II diagram. *Right:* Mid-IR color-color diagram. All the objects fulfilling Stern and/or Jarrett criteria are selected as AGN candidates (189 objects).

mid-IR selected AGN candidates (Fig. 4) are located in the upper part of the star-forming region, near the demarcation line. Only 3 mid-IR selected AGN candidates reside on the AGN region of the BPT diagram, and 4 in the AGN region of the Shirazi He II diagram.

Possible explanations of why AGN candidates found with one selection technique are not selected by the other techniques are discussed in Section 6.

3 AGN FRACTION IN DWARF GALAXIES

As showed in Section 2.2, the fraction of AGN found in the parent sample depends on the considered selection method. About 0.3% of the sample exhibits optical narrow-lines signatures of accreting black holes: 0.1% is selected through BPT diagram while 0.25% through the Shirazi He II diagram. On the other hand, the fraction of galaxies with mid-IR colors attributable to AGN is $\sim 0.4\%$. The comparison between the optical and mid-IR selected AGN samples shows almost no overlap: among 336 AGN candidates, only 3 are selected by all the three selection techniques.

The difference observed between the three samples could be explained from the different biases suffered by the selection criteria (see Section 6 for a discussion). Moreover, a problem in determining the real AGN fraction is the selection function of the sample, which in our case is a consequence of the *SDSS* spectroscopic apparent magnitude limit $r = 17.77$ (petrosian magnitude). In order to perform a reliable demographic analysis we required a magnitude limited sample. Therefore we excluded from the sample all the objects with r -band magnitude $r > 17.77$ mag (see Fig. 1). In this way we excluded 1 BPT selected AGN candidate (out of 48), 9 He II selected AGN candidates (out of 121) and 112 mid-IR selected candidates (out of 189). The high number of mid-IR selected candidates with $r > 17.77$ mag can be explained by the fact that the mid-IR color-color diagram is more sensitive to blue objects (optical colors, see Section 4). These objects were observed by *SDSS* because they were erroneously targeted as quasars.

Fig. 5 shows the AGN percentage in different mass bins.

Green stars refer to AGN candidates selected with BPT diagram, purple hexagons to He II selected AGN candidates, and blue triangles to the mid-IR selected AGN candidates. For each bin we computed the uncertainties of the AGN fraction using binomial statistics. In the cases where less than 20 AGN candidates are in the bin, we computed the uncertainty on the AGN number N_{AGN} using the values reported by Gehrels (1986). For $N_{\text{AGN}} \geq 20$, we applied the formula $\sqrt{f(1-f)N_{\text{tot}}}$, where f is the AGN fraction and N_{tot} the total number of objects in the considered bin. The AGN percentage is $< 2\%$ in each considered bin. For mid-IR selected AGN candidates there is an indication of decreasing fraction with increasing mass. On the other side, BPT and He II selected AGN candidates are found only at higher masses.

4 HOST GALAXY PROPERTIES

We used the galaxy parameters provided by the *SDSS* and *MPA-JHU* catalogs to analyse the properties of the galaxies hosting our AGN candidates. In Fig. 6, 7 and 8 we plotted the distributions of redshift, stellar mass, $[\text{O III}]\lambda 5007$ luminosity, absolute g -band magnitude and $(g-r)$ color for the three samples (BPT selection in green, He II selection in purple, mid-IR selection in blue). As a comparison we also overplotted the distribution for the parent sample (black solid line). The histograms are normalized so that the integral over the bars is unity. For this analysis we considered only objects with absolute r -band magnitude $r < 17.77$. A summary of the results is given in Table 1.

By sample definition, all the considered objects have redshift $z < 0.1$ and stellar mass $M_{\star} \leq 10^{9.5} M_{\odot}$ (Fig. 6). Although we did not put any constraints on a minimum mass, all the objects have stellar mass higher than $M_{\star} = 10^6 M_{\odot}$. This lower limit is a consequence of the *SDSS* spectroscopic flux limit. The redshift distribution is similar for the mid-IR selected AGN and the parent sample, while BPT and He II selected AGN are found only at redshift $z < 0.05$. BPT and

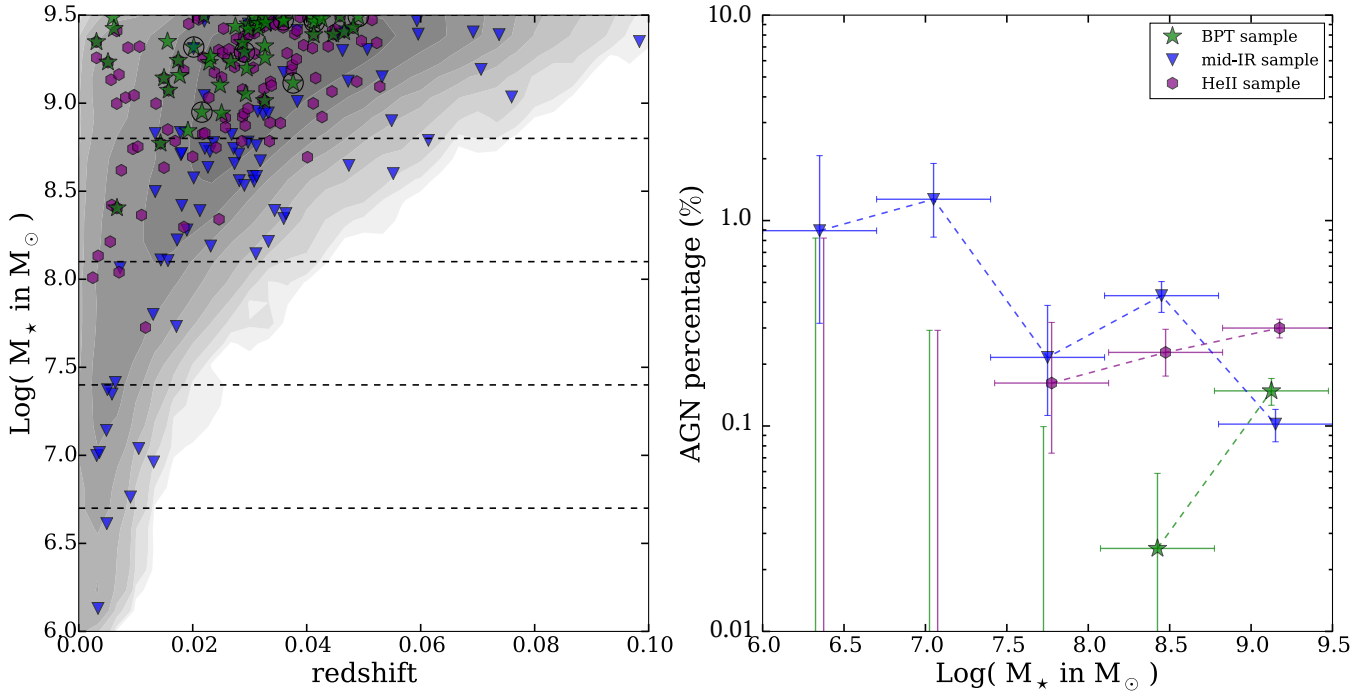


Figure 5. *Left:* Mass versus redshift distribution for the parent sample (gray shaded area) and the AGN candidates. Green stars refer to AGN candidates selected with BPT diagram (the circled stars show the AGN candidates with upper limits for the $H\beta$ flux), purple hexagons to He II selected AGN candidates, and blue triangles to the mid-IR candidates. Only objects with r -band magnitude $r < 17.77$ are considered. The dashed lines divide the sample in five mass bins. *Right:* AGN percentage in the five mass bins defined in the left panel. For each bin we computed the uncertainties of the AGN fraction using binomial statistic (see text for details). The three AGN samples are considered separately.

		BPT sample	He II sample	mid-IR sample	parent sample
Redshift	$\langle z \rangle$	0.028	0.027	0.030	0.031
Stellar mass in M_\odot	$\langle \log(M_*) \rangle$	9.28	9.09	8.55	8.97
[O III] λ 5007 luminosity in erg/s	$\langle \log(L_{[\text{O III}]}) \rangle$	39.53	39.43	39.85	39.23
g -band magnitude in mag	$\langle M_g \rangle$	-17.90	-18.13	-17.68	-18.01
$(g-r)$ color in mag	$\langle (g-r) \rangle$	0.57	0.41	0.21	0.39

Table 1. Mean values of the host galaxy properties showed in Fig. 6, 7 and 8. Values are given for the three AGN samples and for the parent sample separately. Only objects with absolute r -band magnitude $r < 17.77$ are considered.

He II selected AGN are found at higher masses compared to the mid-IR sample.

The [O III] λ 5007 luminosity distribution (Fig. 7, top panel) is similar for the BPT and He II AGN candidates, while mid-IR AGN candidates appear to have also higher luminosity. For this plot we considered only objects with $\text{AON} > 3$ for the [O III] λ 5007 line.

The mean absolute g -band magnitude (Fig. 7, bottom panel) is similar for the three samples of AGN candidates and for the total sample. For this analysis we considered the petrosian magnitude, corrected for galactic foreground extinction.

Fig. 8 shows the $(g-r)$ color distribution. Also in this case the *SDSS* magnitudes are corrected for galactic foreground extinction. BPT selected AGN show redder optical colors compared to the parent sample, while the mid-IR selected AGN are bluer. Similar to the BPT selected AGN candidates, He II selected AGN candidates show redder

colors compared to the mid-IR selected ones, but they are still bluer than the BPT selected AGN candidates. The difference in color is also noticed in the *SDSS* images shown in Fig. 9.

In the previous analysis we looked at each parameter separately. However, most of these parameters are correlated with each other, and a simple histogram comparison can be misleading. For this reason we plotted the 2D relations of some of these quantities (see Appendix B). In all the cases the BPT and He II selected AGN seem to separate from most of the mid-IR sample on the 2D planes (stellar mass versus $(g-r)$, [O III] luminosity and g -band magnitude, see Figures B1 – B3). This suggests that mid-IR and optical selection criteria select two different classes of AGN host galaxies.

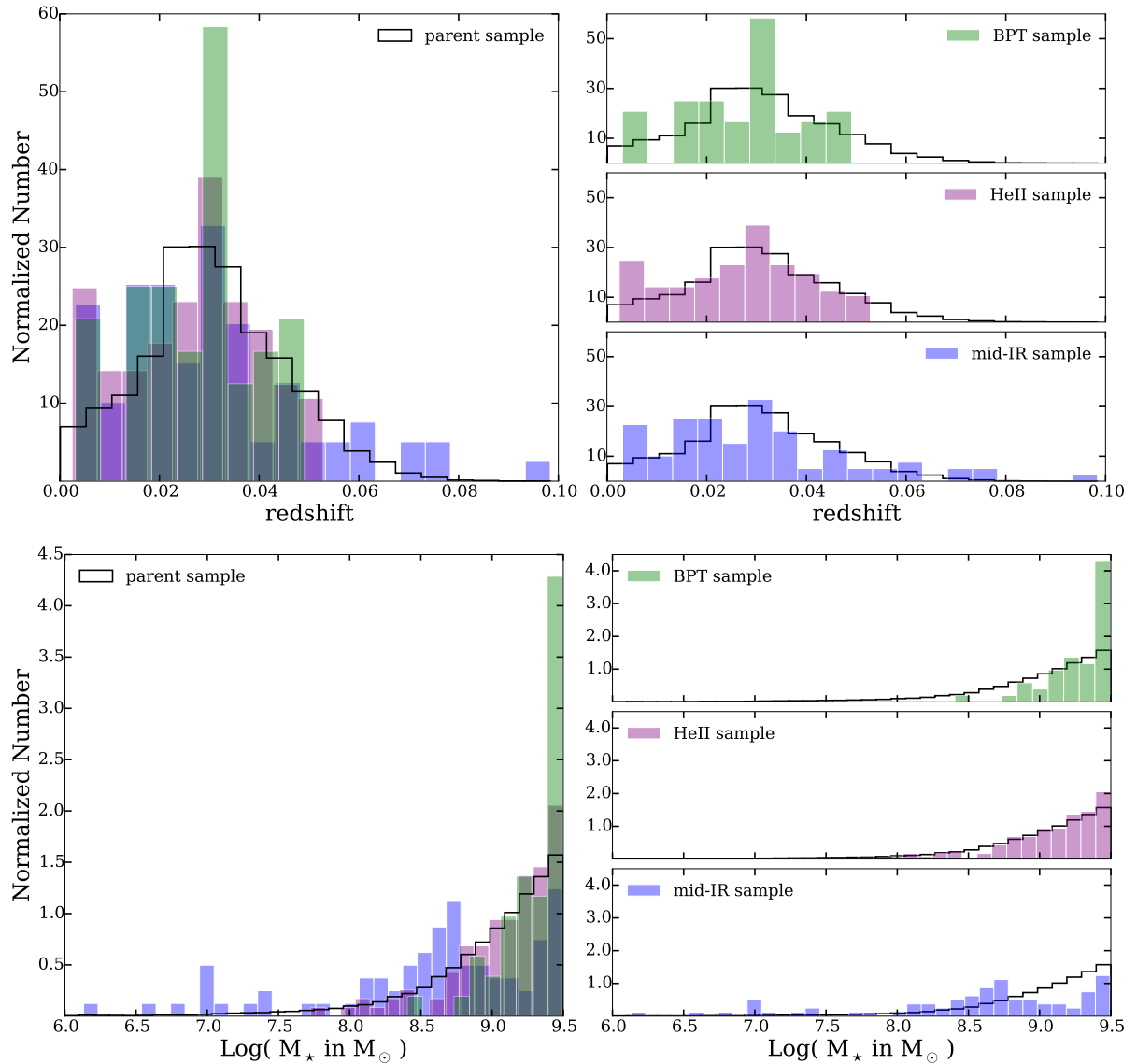


Figure 6. Redshift (top panels) and stellar mass (bottom panels) distributions for the three samples of AGN candidates. The BPT sample is shown in green, the He II sample in purple and the mid-IR sample in blue. The black solid line corresponds to the parent sample. The histograms are normalized so that the integral over the bars is unity. Only objects with absolute r -band magnitude $r < 17.77$ are considered.

5 X-RAY AND RADIO ANALYSIS

Optical emission line diagnostic and mid-IR color selection provided a sample of 336 AGN candidates. However, high resolution follow-up observations at other wavelengths are required for the confirmation of AGN activity in these objects. We searched the *Chandra* Data Archive⁶ and the *VLA FIRST* Survey Catalog⁷ (Becker, White & Helfand 1994) to get X-ray and radio observations of our sources.

We obtained archival *Chandra* X-ray data for 11 objects in our sample (objects 5426, 94970, 166401, 230467, 306717, 190553, 338999, 12974, 54437, 5424 and 69465).

⁶ <http://cda.harvard.edu/chaser/>

⁷ <http://sundog.stsci.edu>

Only one source, object 69465, is detected with enough counts to extract the spectrum and fit it. This source shows a soft spectrum, which can be best fitted with the *Xspec* model *diskbb* with temperature $kT \sim 0.35$ keV.

For the other sources with faint detections we computed the hardness ratio (HR) from the counts in the soft (0.5 – 2.0 keV) and hard (2.0 – 8.0 keV) bands. Apart from object 5424, which shows an HR of 0.6, all the other sources are soft with HR smaller than -0.1 . For these faint sources we estimated the flux in the 0.5 – 2.0 keV range using *WebPIMMS*, which we used to convert the measured 0.5 – 2.0 keV *Chandra* count rate into flux. We repeated the calculations for both *diskbb* and *powerlaw* models, but the result does not change significantly.

Fig. 10 shows the 0.5 – 2.0 keV X-ray luminosity as a function of $H\alpha$ luminosity. The dashed line corresponds

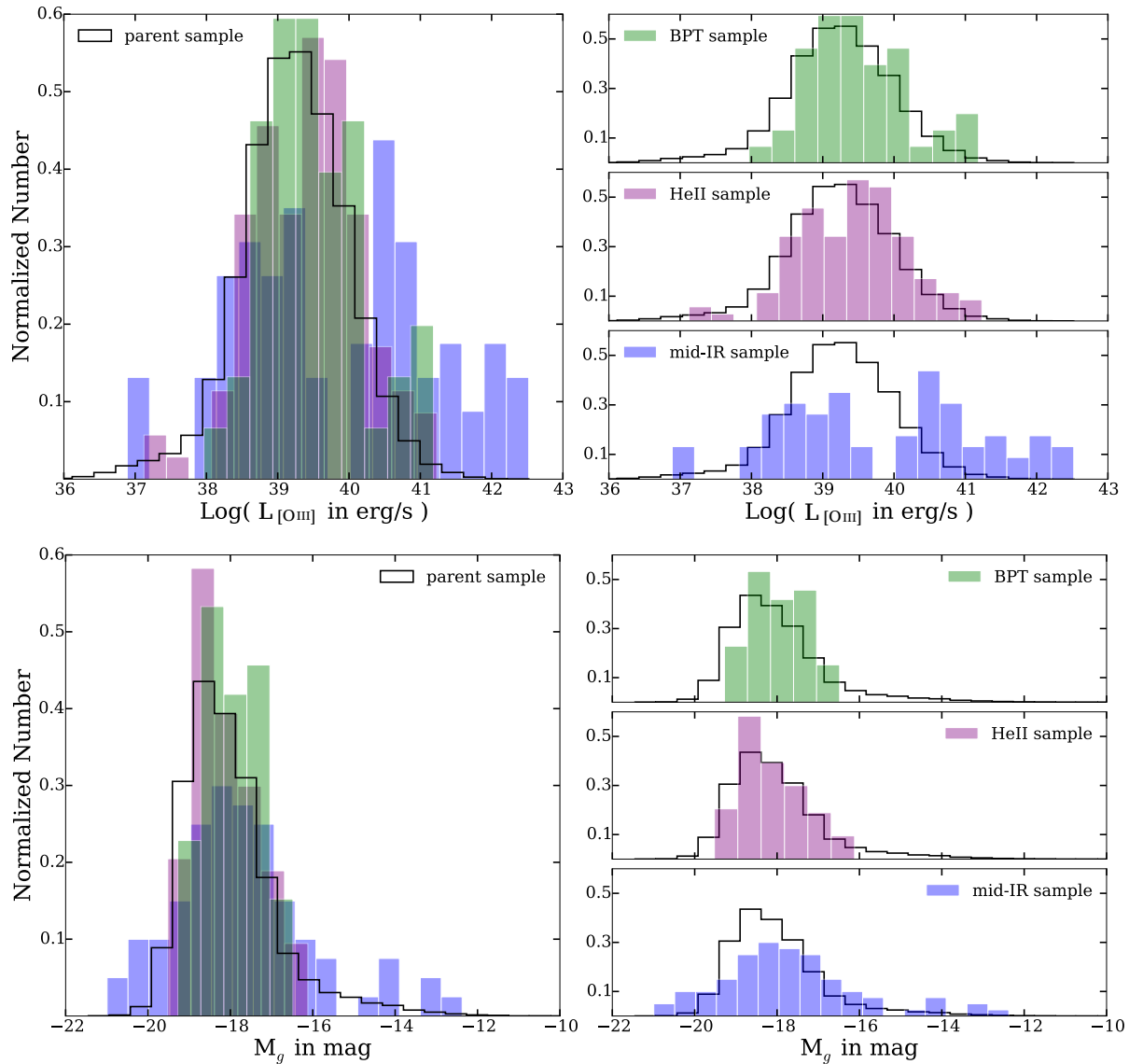


Figure 7. Same as Fig. 6 but for $[\text{O III}]\lambda 5007$ luminosity (top panels) and absolute g -band magnitude (bottom panels). For the $[\text{O III}]\lambda 5007$ distribution we considered only objects with $\text{AON} > 3$ for that line. For the absolute g -band magnitude distribution we considered the petrosian magnitude which we corrected for galactic foreground extinction.

to the expected X-ray luminosity assuming that all the $\text{H}\alpha$ luminosity comes from star formation. We computed this line from the $\text{SFR} - L(0.5 - 2.0 \text{ keV})$ relation given in Ranalli, Comastri & Setti (2003), and the $\text{SFR} - L(\text{H}\alpha)$ relation given in Kennicutt, Tamblyn & Congdon (1994). For the four BPT and/or HeII AGN candidates the observed X-ray luminosities exceed the luminosity expected by pure star formation by at least one order of magnitude. This is a confirmation of AGN activity. In the case of mid-IR selected AGN the observed X-ray emission could come from star formation, and we cannot rule out the possibility that these objects are indeed pure star-forming galaxies.

The *VLA FIRST Survey Catalog* provided us the radio 1.4 GHz fluxes of 12 AGN candidates (5424, 84989, 92048, 54437, 60324, 72486, 94970, 115666, 190553, 221600, 50838 and 26813). Fig. 11 shows the same as

Fig. 10 but for radio instead of X-ray luminosity. Here we assumed the $\text{SFR} - L(1.4 \text{ GHz})$ relation given in Yun, Reddy & Condon (2001). Similarly to what is seen in the X-ray analysis, the radio luminosity of BPT and/or HeII selected AGN candidates is at least one order of magnitude higher compared to what expected from stellar emission only, confirming the AGN activity. The radio luminosity seems to confirm the AGN presence also in at least three, probably four of the mid-IR AGN candidates (one of them selected also through emission line diagnostic).

The X-ray and radio analysis presented here are preliminary results, based on the few AGN candidates with archival X-ray and/or radio data. We are currently acquiring *XMM-Newton* observations of some of the AGN candidates, and a more complete analysis will be presented in a following paper (Sartori et al. in prep.).

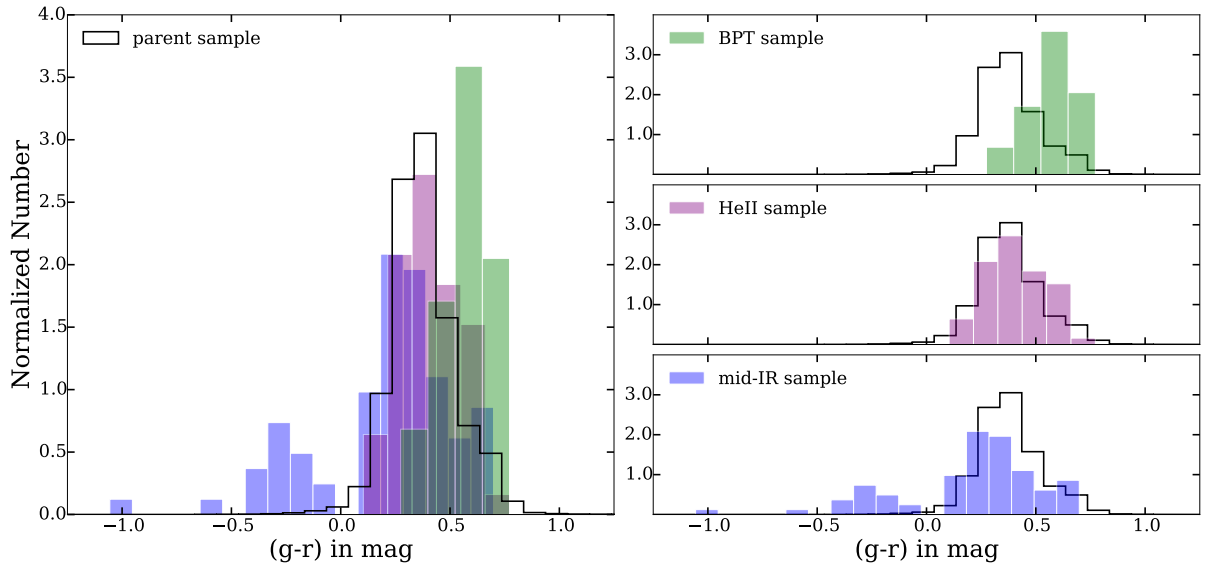


Figure 8. Same as Fig. 6 but for the optical $(g-r)$ color. We considered the petrosian g - and r -band magnitudes which we corrected for galactic foreground extinction.

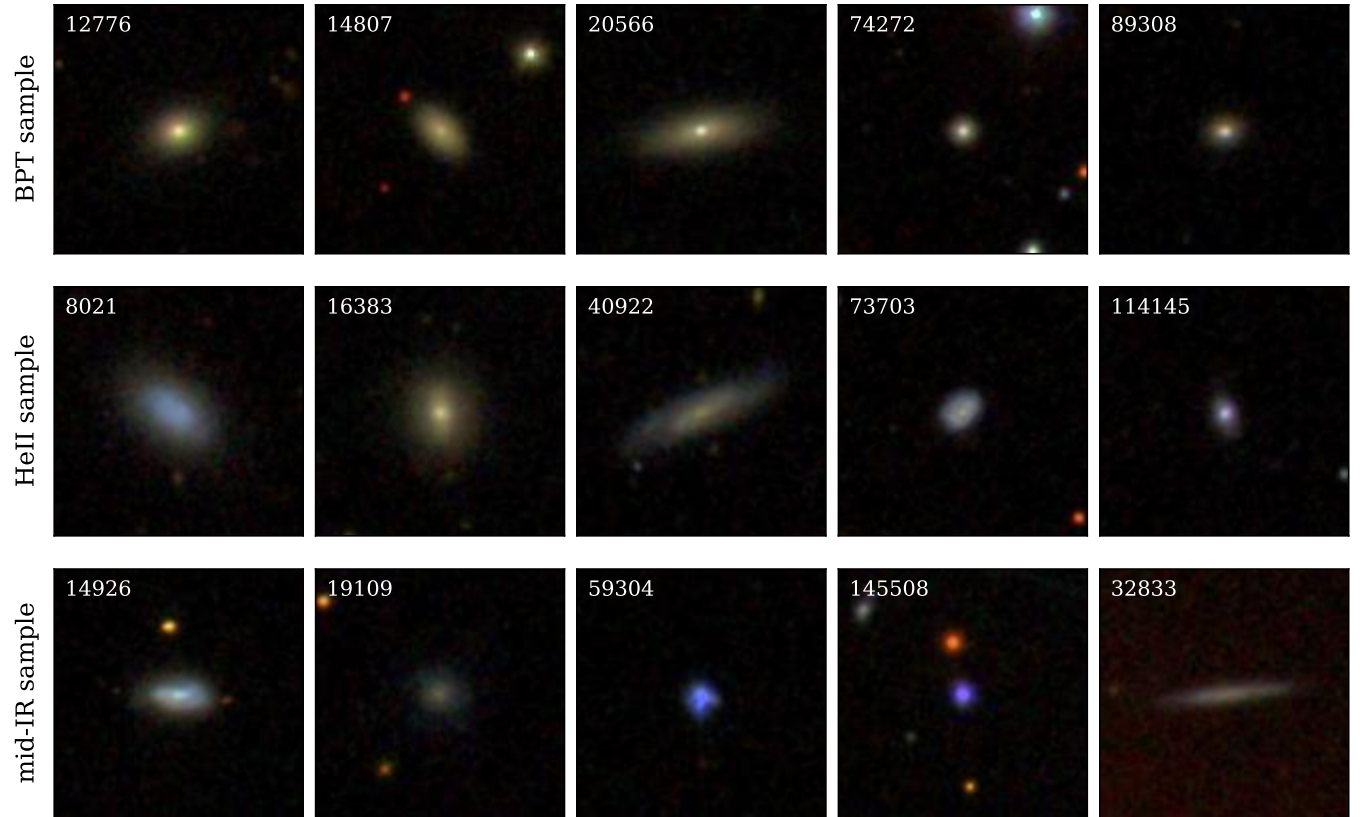


Figure 9. Composite images of some of the AGN host galaxies for AGN selected with different techniques. The images are taken from *SDSS* and the size is 50×50 arcseconds. *Top*: BPT selection, *Middle*: HeII selection, *Bottom*: mid-IR selection.

6 DISCUSSION

6.1 AGN selection and host galaxy properties

In this study we selected AGN in nearby dwarf galaxies using three different selection techniques, and analysed their host galaxy properties.

BPT selection provides 48 AGN candidates. Compared to the total sample, the galaxies hosting these AGN are found mostly at higher masses and low redshift. Moreover, they show redder optical colors. The high masses and red colors of the objects in this sample are consistent with what presented in Moran et al. (2014). Yet, there are a number

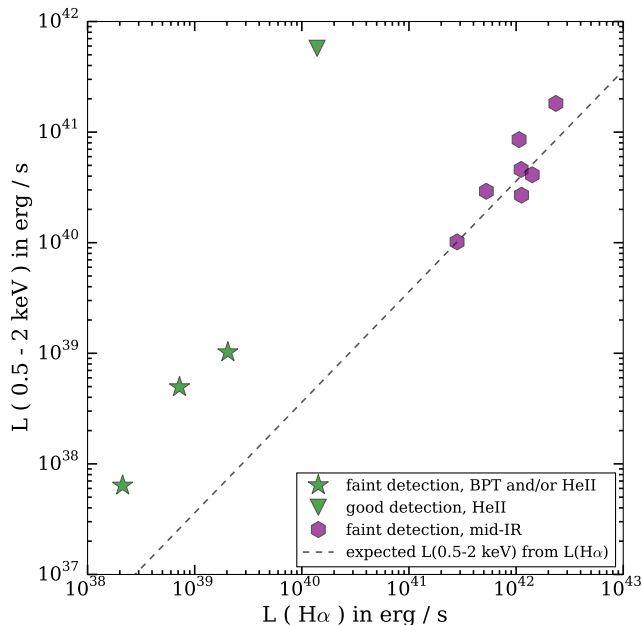


Figure 10. 0.5 – 2.0 keV X-ray luminosity as a function of $H\alpha$ luminosity. The dashed line corresponds to the expected X-ray luminosity assuming that all the $H\alpha$ luminosity comes from star formation. This line was computed from the SFR – $L(0.5 - 2.0$ keV) relation given in Ranalli, Comastri & Setti (2003), and the SFR – $L(H\alpha)$ relation given in Kennicutt, Tamblyn & Congdon (1994). Green points correspond to BPT and/or HeII selected AGN candidates (the stars represent the faint detections while the triangle represents the only good detection, for which it was possible to extract the X-ray spectrum), while purple hexagons represent the mid-IR selected AGN candidates.

of obstacles preventing us from detecting all the AGN in the sample using the BPT diagram. The observed trends in mass and color could therefore be attributable to selection effects and biases arising from observing strategy and detection method. The observing strategy biases are due to the fact that AGN in dwarf galaxies selected via the *SDSS* spectra can suffer from fiber aperture effects: since dwarf galaxies are small in the sky, a big fraction of their light falls within the *SDSS* fiber. AGN in blue star-forming low-mass dwarf galaxies may not be detected since the observed emission is dominated by galaxy light (from star formation), causing the BPT sample to be biased towards redder, more massive galaxies. Regarding the biases due to detection method, both theoretical and observational studies shows that AGN in low-metallicity galaxies, which are mainly low-mass star-forming galaxies (e.g. Groves, Heckman & Kauffmann 2006; Panter et al. 2008), move to the left-hand side of the $[N\text{II}]/H\alpha$ BPT diagram and cannot be distinguished from pure star-forming galaxies (e.g. Groves, Heckman & Kauffmann 2006; Kewley et al. 2013).

Applying the HeII selection diagram proposed by Shirazi & Brinchmann (2012), we identified 121 AGN candidates. All the BPT selected candidates with well detected HeII lines (18) are selected also with the Shirazi HeII diagram. The host galaxies of the HeII selected AGN candidates show properties similar to the BPT selected ones. In particular, they have redder colors and higher masses compared to the parent sample and to the mid-IR selected AGN

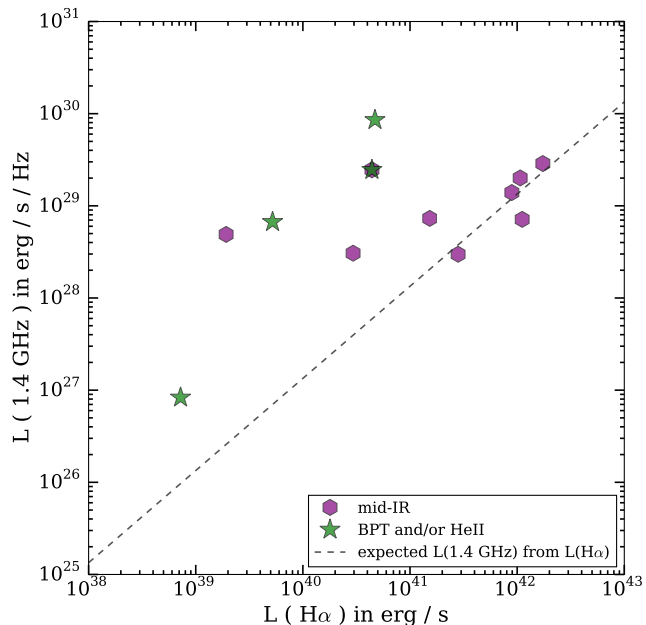


Figure 11. 1.4 GHz radio luminosity as a function of $H\alpha$ luminosity. The dashed line corresponds to the expected radio luminosity assuming that all the $H\alpha$ luminosity comes from star formation. This line was computed from the SFR – $L(1.4$ GHz) relation given in Yun, Reddy & Condon (2001), and the SFR – $L(H\alpha)$ relation given in Kennicutt, Tamblyn & Congdon (1994). Green stars correspond to BPT and/or HeII selected AGN candidates, while purple hexagons represent the mid-IR selected AGN candidates.

sample. However, they are slightly bluer and less massive compared to the BPT selected sample, what could suggest that they are subject to a higher star formation (higher sSFR). Since $[O\text{III}]$ is more affected by star formation compared to HeII, this may be the reason why most of the HeII selected galaxies are not found in the AGN region of the BPT diagram. Thus, the Shirazi HeII diagram appears to be more sensitive to AGN hosted in star-forming galaxies than the classical BPT diagram, at least in the low-mass regime. The disadvantage of this selection technique is that the HeII line is fainter compared to the $[O\text{III}]$ line, and can be well detected only in a much smaller sample.

The 189 mid-IR selected AGN candidates are found preferentially at low-masses compared to the parent sample, and show bluer optical colors. This is an indication of strong ongoing star formation. Blue colors could also signify the presence of an unobscured AGN, in which case broad $H\alpha$ lines should be visible. However, we checked the optical spectra and none of the mid-IR selected AGN candidates show broad $H\alpha$ lines. Similar to what is seen for the BPT selection, mid-IR selection is affected by important, but distinct, biases. As explained in Stern et al. (2012), for heavily obscured low-redshift AGN or objects dominated by stellar emission the dilution by the host galaxy may cause a bluer ($W1 - W2$) color, so that these AGN move toward the galaxy locus and cannot be separated from star-forming galaxies. In order to test the sensitivity of mid-IR color selection we performed simulations, and found that only objects with AGN contributing at least 10 – 20%

to the total bolometric luminosity can be detected using mid-IR color-color diagram.

A comparison between optical emission lines (BPT and He II) and mid-IR selection techniques shows almost no overlap (3/336 objects). Most of the BPT and He II selected AGN are selected as pure star-forming galaxies when applying the mid-IR color criterion. On the other hand, most of the mid-IR selected AGN candidates are located in the upper part of the star-forming region of the BPT diagram, near to the pure starburst demarcation line defined by Kewley et al. (2001), and on the star-forming region of the Shirazi He II diagram. The two samples exhibit also different host galaxy properties. In summary, the mid-IR sample is both bluer and with lower stellar masses, while the optical emission lines selected sample is redder with higher stellar masses.

One reason why mid-IR selected AGN are not selected by BPT diagram could be strong ongoing star formation. Although star formation could potentially affect both techniques, it is important to note that the biases due to observing strategy and detection method described for the BPT selection are not affecting the mid-IR selection. This means that star-formation may be affecting the BPT selection more than the mid-IR selection, explaining why the mid-IR selected AGN sample is bluer than the BPT selected one. The observation that He II selected AGN are bluer than the BPT selected ones (but still redder than the mid-IR selected AGN) is a consequence of the fact that [O III] is more sensitive to star formation than He II. Therefore, some objects can be selected as AGN using the Shirazi He II diagram, but the star formation is still too high to allow a selection using standard BPT diagram.

Another possible explanation of the fact that mid-IR selected AGN are bluer is that they contain less metals. Kewley et al. (2013) showed that AGN are hard to distinguish from star-forming galaxies using the BPT diagram for metallicities lower than $\log(O/H) + 12 \sim 8.4$, and $\sim 50\%$ of the mid-IR selected AGN are below this threshold. This is suggestive that the mid-IR selection is more sensitive to detecting low-mass, low metallicity AGN host galaxies compared to optical emission lines selection.

6.1.1 *The mid-IR selected AGN revisited: how many of them are AGN?*

The X-ray and radio observations available for some of the AGN candidates selected through optical emission line diagnostic confirm the AGN nature of these sources. Moreover, the BPT and He II regions correspondent to AGN are unlikely to be contaminated by other types of galaxies. Thus, we assume that the BPT and He II selected AGN candidates are indeed AGN.

The mid-IR selection could be contaminated by non-AGN. Stern et al. (2012) claim a reliability of 95% at quasar luminosities but it is unclear to what degree this is the case for low-luminosity AGN. An alternative source of the mid-IR emission, as opposed to light reprocessed by the obscuring torus and reemitted at longer wavelengths, is free-free

emission from young stars present in extreme star-forming galaxies (e.g. Leitherer et al. 1999). This emission could in principle light up the dust in the galaxy in a similar way as seen in AGN. Possible contaminants are low metallicity blue compact dwarfs (e.g. Griffith et al. 2011), ultraluminous infrared galaxies (e.g. Jarrett et al. 2011), and objects similar to the Green Peas discussed in Cardamone et al. (2009).

Four of the mid-IR selected AGN also show optical signature of BH accretion. In addition, the available radio data seem to confirm the AGN presence in at least other three objects. Thus, we know that at least some of the mid-IR selected AGN candidates are indeed AGN. However, with our analysis we cannot rule out the possibility that part of these objects are not AGN. Follow up studies, especially aiming to acquire better X-ray data for a larger part of the sample, are needed to better understand the mid-IR selection in dwarf galaxies and confirm the AGN nature of the candidates. If some of the AGN candidates selected according to the mid-IR criteria are indeed pure star-forming galaxies, then this could further explain the bluer colors observed in these objects compared to the optically selected AGN. Moreover, it would imply a still lower AGN fraction in nearby low-mass galaxies.

6.2 AGN fraction in dwarf galaxies

The measured AGN fraction depends on the selection technique. About 0.1% of the parent sample can be selected as AGN using the BPT diagram. This value is consistent with what found by Reines, Greene & Geha (2013), where they selected 35 AGN candidates out of a sample of $\sim 25,000$ objects ($\sim 0.13\%$). On the other hand, the value is lower compared to what found by Moran et al. (2014), but this is due to a different selection of the parent sample. By considering also He II selected AGN candidates, the fraction of objects exhibiting optical signatures of BH accretion increases to $\sim 0.3\%$. The fraction of galaxies with mid-IR colors attributable to AGN is $\sim 0.4\%$. If all the candidates are confirmed to be AGN, this means that the mid-IR detection rate is higher than optical detection rate. For higher masses (above $\sim 10^{9.5} M_{\odot}$) the AGN occupation fraction determined from BPT selection is expected to be $\sim 5 - 10\%$ (e.g. Kauffmann et al. 2003a). Yet, including all AGN candidates found by different techniques the occupation fraction in the low-mass regime is low measured with optical and mid-IR selection techniques, $\sim 0.7\%$. This is at least one order of magnitude below what found for more massive galaxies, what could signify that 1) with the applied selection techniques we are missing an high number of AGN hosted in low-mass galaxies; or 2) the low-mass galaxies are less likely to host active BHs compared to more massive objects. Since AGN are active BHs, the second option could be due to a very low BH occupation fraction, which would imply also a low AGN fraction, or to a low fraction of active BHs among all the existing BHs (in this case the BH occupation fraction could still be comparable to what found at higher mass regime).

The AGN fraction for mid-IR selected AGN shows a small decrease for increasing stellar mass, as reported also in Satyapal et al. (2014) and Marleau et al. (2014). However,

in each bin the fraction is small compared to the values found for more massive galaxies ($< 2\%$), and the trend is not as strong as claimed by Satyapal et al. (2014). On the other hand, the AGN fraction for optically selected AGN increases with increasing mass. The trend showed by the optically selected AGN is consistent with what found for more massive galaxies (e.g. Kauffmann et al. 2003a). On the other hand, the decrease seen for mid-IR selected AGN candidates could signify that in galaxies with higher stellar masses the AGN is not powerful enough to dominate over the host galaxy emission, at least in the mid-IR.

6.2.1 Possible consequences for BH formation scenarios

Models of BH growth in a cosmological context suggest a different BH occupation fraction in the low-mass regime for different seed formation scenarios. It has therefore been proposed that measuring the BH occupation fraction in dwarf galaxies may help in discriminating between seed formation scenarios (e.g. Volonteri, Lodato & Natarajan 2008; see also Reines, Greene & Geha 2013 and Moran et al. 2014). Since BHs in dwarf galaxies can be detected only if they are accreting (AGN), we cannot directly measure the BH occupation fraction, but we can put a lower limit on it by measuring the AGN fraction. With this study we measured a lower limit for the BH occupation fraction below 1%. Despite progress, the current models are still unprecise and do not allow to estimate precisely the expected BH occupation fraction, however the difference between seed formation scenarios in general plays a role at high BH occupation fractions, which cannot be constrained by a lower limit smaller than 1%. Thus, the approach of using the AGN fraction to constrain BH seed formation models, regardless of the precise predictions of the models, is unlikely to succeed.

7 SUMMARY

We systematically searched for AGN in a sample of 48,416 nearby low-mass galaxies ($M_* < 10^{9.5} M_\odot$, $z < 0.1$) selected from the *SDSS* catalog. Using optical emission line diagnostic diagrams (classical BPT selection and the He II diagram presented in Shirazi & Brinchmann 2012) and mid-IR selection we assembled a sample of 336 AGN candidates. The main results of this work can be summarized as follows:

- The fraction of AGN in nearby dwarf galaxies selected using optical emission line diagnostic diagrams (BPT and He II) is $\sim 0.3\%$. For mid-IR selection the AGN fraction is $\sim 0.4\%$. By considering all the found AGN candidates together, the observed AGN fraction in the low-mass regime seems to be at least one order of magnitude below what found for more massive objects (see e.g. Kauffmann et al. 2003a). Moreover, the obtained AGN fraction, which is a lower limit for the BH occupation fraction in the low-mass regime, does not allow us to put strong limits on the BH occupation fraction and to constrain currently proposed seed formation scenarios.

- Mid-IR selection and optical emission lines selection (BPT and He II) revealed two different samples of AGN candidates. Among 336 AGN candidates, only 3 are

selected by all the three criteria. The AGN candidates samples show different physical properties, what could signify also different nature. Mid-IR selected AGN are both bluer (optical color) and with lower stellar mass. This could be an indication of low metallicity and strong ongoing star formation. On the other hand, AGN selected by the BPT diagram are redder and with higher stellar mass. He II selected AGN candidates are bluer compared to the BPT selected candidates, but still redder than the mid-IR selected sample. The difference in mass and color observed for the two samples could in part be a consequence of biases due to observing strategy and detection method. These biases could prevent to detect AGN in blue star-forming low-mass galaxies by applying BPT selection.

- The optical emission line diagnostic diagram based on He II $\lambda 4686$ proposed by Shirazi & Brinchmann (2012) appears to be more sensitive to AGN hosted in star-forming galaxies than the classical BPT diagram, at least in the low-mass regime.

- The archival X-ray and radio data available for some of the BPT and/or He II selected AGN candidates confirm the AGN nature of these sources. However, it is not possible to confirm that all the mid-IR selected AGN candidates are indeed AGN. A possible alternative source of the observed mid-IR emission is free-free emission from young stars present in extreme star-forming galaxies. This could further explain the bluer colors showed by the mid-IR selected AGN candidates compared to the ones found with optical emission lines selections. Follow-up observations, especially in the X-rays, are needed to confirm the AGN nature of these sources.

- We compiled a sample of AGN candidates which will be important for future follow-up studies aiming to understand the relation between BHs and host galaxies in the low-mass regime.

This work confirmed that AGN can indeed be found in low-mass galaxies (see also e.g. Reines, Greene & Geha 2013, Moran et al. 2014). Because of selection biases no selection technique based on a single wavelength range allows for a perfectly unbiased sample. Thus, only the combination of data at different wavelengths will provide us information about the nature of BHs and the relation with their host galaxies in the low-mass regime. More follow-up observations are needed to confirm the AGN nature of all the found candidates and to understand their properties.

ACKNOWLEDGMENTS

We thank the referee for helpful comments, and Marta Volonteri and Michael R. Meyer for useful discussions. LFS, KS and MK gratefully acknowledge support from Swiss National Science Foundation Professorship grant PP00P2_138979/1 and MK support from SNSF Ambizione grant PZ00P2_154799/1. LFS gratefully acknowledges financial support from the Swiss Study Foundation. Support for the work of ET was provided by the Center of Excellence in Astrophysics and Associated Technologies

(PFB 06), by the FONDECYT regular grant 1120061 and by the CONICYT Anillo project ACT1101. KO was supported by the National Research Foundation of Korea (Doyak 2014003730). KO was a Swiss Government Excellence Scholarship holder for the academic year 2013-2014 (ESKAS No.2013.0308)

This research has made use of NASA's ADS service, and of data products from *SDSS*, *WISE*, *2MASS*, *Chandra* and *VLA FIRST*. Funding for the SDSS and SDSS-II has been provided by the Alfred P. Sloan Foundation, the Participating Institutions, the National Science Foundation, the U.S. Department of Energy, the National Aeronautics and Space Administration, the Japanese Monbukagakusho, the Max Planck Society, and the Higher Education Funding Council for England. The SDSS Web Site is <http://www.sdss.org/>. The SDSS is managed by the Astrophysical Research Consortium for the Participating Institutions. The Participating Institutions are the American Museum of Natural History, Astrophysical Institute Potsdam, University of Basel, University of Cambridge, Case Western Reserve University, University of Chicago, Drexel University, Fermilab, the Institute for Advanced Study, the Japan Participation Group, Johns Hopkins University, the Joint Institute for Nuclear Astrophysics, the Kavli Institute for Particle Astrophysics and Cosmology, the Korean Scientist Group, the Chinese Academy of Sciences (LAMOST), Los Alamos National Laboratory, the Max-Planck-Institute for Astronomy (MPIA), the Max-Planck-Institute for Astrophysics (MPA), New Mexico State University, Ohio State University, University of Pittsburgh, University of Portsmouth, Princeton University, the United States Naval Observatory, and the University of Washington. We are grateful to the MPA/JHU group for access to their data products and catalogues (maintained by Jarle Brinchmann at <http://www.mpa-garching.mpg.de/SDSS/>). The Wide-field Infrared Survey Explorer is a joint project of the University of California, Los Angeles, and the Jet Propulsion Laboratory/California Institute of Technology, funded by the National Aeronautics and Space Administration. The Two Micron All Sky Survey is a joint project of the University of Massachusetts and the Infrared Processing and Analysis Center/California Institute of Technology, funded by the National Aeronautics and Space Administration and the National Science Foundation. This research has made use of data obtained from the Chandra Data Archive and the Chandra Source Catalog, and software provided by the Chandra X-ray Center (CXC) in the application package CIAO.

REFERENCES

- Abazajian K. N. et al., 2009, *ApJS*, 182, 543
 Alonso-Herrero A., Rieke M. J., Rieke G. H., Shields J. C., 2000, *ApJ*, 530, 688
 Assef R. J. et al., 2010, *ApJ*, 713, 970
 Assef R. J. et al., 2012, *ArXiv e-prints*
 Baldwin J. A., Phillips M. M., Terlevich R., 1981, *PASP*, 93, 5
 Barth A. J., Shields J. C., 2000, *PASP*, 112, 753
 Becker R. H., White R. L., Helfand D. J., 1994, in *Astronomical Society of the Pacific Conference Series*, Vol. 61, *Astronomical Data Analysis Software and Systems III*, Crabtree D. R., Hanisch R. J., Barnes J., eds., p. 165
 Begelman M. C., Volonteri M., Rees M. J., 2006, *MNRAS*, 370, 289
 Bellovary J., Volonteri M., Governato F., Shen S., Quinn T., Wadsley J., 2011, *ApJ*, 742, 13
 Bentz M. C., Peterson B. M., Pogge R. W., Vestergaard M., 2009, *ApJ*, 694, L166
 Brinchmann J., Charlot S., White S. D. M., Tremonti C., Kauffmann G., Heckman T., Brinkmann J., 2004, *MNRAS*, 351, 1151
 Bromm V., Coppi P. S., Larson R. B., 1999, *ApJ*, 527, L5
 Bromm V., Yoshida N., 2011, *ARA&A*, 49, 373
 Cardamone C. et al., 2009, *MNRAS*, 399, 1191
 Cutri R. M., et al., 2012, *VizieR Online Data Catalog*, 2311, 0
 Desroches L.-B., Ho L. C., 2009, *ApJ*, 690, 267
 Diamond-Stanic A. M., Rieke G. H., Rigby J. R., 2009, *ApJ*, 698, 623
 Dong X.-B., Ho L. C., Yuan W., Wang T.-G., Fan X., Zhou H., Jiang N., 2012, *ApJ*, 755, 167
 Dopita M. A., Sutherland R. S., 1995, *ApJ*, 455, 468
 Elitzur M., Shlosman I., 2006, *ApJ*, 648, L101
 Elvis M. et al., 1994, *ApJS*, 95, 1
 Ferrarese L., Merritt D., 2000, *ApJ*, 539, L9
 Filippenko A. V., Terlevich R., 1992, *ApJ*, 397, L79
 Gallo E., Treu T., Jacob J., Woo J.-H., Marshall P. J., Antonucci R., 2008, *ApJ*, 680, 154
 Gallo E., Treu T., Marshall P. J., Woo J.-H., Leipski C., Antonucci R., 2010, *ApJ*, 714, 25
 Gebhardt K. et al., 2000, *ApJ*, 539, L13
 Gehrels N., 1986, *ApJ*, 303, 336
 Ghosh H., Mathur S., Fiore F., Ferrarese L., 2008, *ApJ*, 687, 216
 Goulding A. D., Alexander D. M., Lehmer B. D., Mullaney J. R., 2010, *MNRAS*, 406, 597
 Greene J. E., 2012, *Nature Communications*, 3
 Greene J. E., Ho L. C., 2004, *ApJ*, 610, 722
 Greene J. E., Ho L. C., 2007, *ApJ*, 670, 92
 Griffith R. L. et al., 2011, *ApJ*, 736, L22
 Groves B. A., Heckman T. M., Kauffmann G., 2006, *MNRAS*, 371, 1559
 Gultekin K., 2009, *ArXiv e-prints*
 Haehnelt M. G., Rees M. J., 1993, *MNRAS*, 263, 168
 Heckman T. M., 1980, *A&A*, 87, 152
 Heckman T. M., Kauffmann G., Brinchmann J., Charlot S., Tremonti C., White S. D. M., 2004, *ApJ*, 613, 109
 Ho L. C., 2008, *ARA&A*, 46, 475
 Jarrett T. H. et al., 2011, *ApJ*, 735, 112
 Kamizasa N., Terashima Y., Awaki H., 2012, *ApJ*, 751, 39
 Kauffmann G. et al., 2003a, *MNRAS*, 346, 1055
 Kauffmann G. et al., 2003b, *MNRAS*, 341, 33
 Kennicutt, Jr. R. C., Tamblyn P., Congdon C. E., 1994, *ApJ*, 435, 22
 Kewley L. J., Dopita M. A., Leitherer C., Davé R., Yuan T., Allen M., Groves B., Sutherland R., 2013, *ApJ*, 774, 100
 Kewley L. J., Dopita M. A., Sutherland R. S., Heisler C. A., Trevena J., 2001, *ApJ*, 556, 121

- Kewley L. J., Groves B., Kauffmann G., Heckman T., 2006, *MNRAS*, 372, 961
- Kormendy J., Ho L. C., 2013, *ARA&A*, 51, 511
- Kormendy J., Richstone D., 1995, *ARA&A*, 33, 581
- Koss M., Mushotzky R., Veilleux S., Winter L. M., Baumgartner W., Tueller J., Gehrels N., Valencic L., 2011, *ApJ*, 739, 57
- Lacy M. et al., 2004, *ApJS*, 154, 166
- Lamastra A., Bianchi S., Matt G., Perola G. C., Barcons X., Carrera F. J., 2009, *A&A*, 504, 73
- Leitherer C. et al., 1999, *ApJS*, 123, 3
- Lodato G., Natarajan P., 2006, *MNRAS*, 371, 1813
- Ludwig R. R., Greene J. E., Barth A. J., Ho L. C., 2012, *ApJ*, 756, 51
- Maoz D., Koratkar A., Shields J. C., Ho L. C., Filippenko A. V., Sternberg A., 1998, *AJ*, 116, 55
- Marconi A., Hunt L. K., 2003, *ApJ*, 589, L21
- Marleau F. R., Clancy D., Bianconi M., Habas R., 2014, *ArXiv e-prints*
- Miller B., Gallo E., Treu T., Woo J.-H., 2012, *ApJ*, 747, 57
- Moran E. C., Filippenko A. V., Chornock R., 2002, *ApJ*, 579, L71
- Moran E. C., Shahinyan K., Sugarman H. R., Velez D. O., Eracleous M., 2014, *ArXiv e-prints*
- Netzer H., 2009, *MNRAS*, 399, 1907
- Oh K., Sarzi M., Schawinski K., Yi S. K., 2011, *ApJS*, 195, 13
- Panessa F., Wolter A., Pellegrini S., Fruscione A., Bassani L., Della Ceca R., Palumbo G. G. C., Trinchieri G., 2005, *ApJ*, 631, 707
- Panter B., Jimenez R., Heavens A. F., Charlot S., 2008, *MNRAS*, 391, 1117
- Ranalli P., Comastri A., Setti G., 2003, *A&A*, 399, 39
- Reines A. E., Greene J. E., Geha M., 2013, *ApJ*, 775, 116
- Sarzi M. et al., 2010, *MNRAS*, 402, 2187
- Satyapal S., Böker T., McAlpine W., Gliozzi M., Abel N. P., Heckman T., 2009, *ApJ*, 704, 439
- Satyapal S., Secrest N. J., McAlpine W., Ellison S. L., Fischer J., Rosenberg J. L., 2014, *ArXiv e-prints*
- Satyapal S., Vega D., Dudik R. P., Abel N. P., Heckman T., 2008, *ApJ*, 677, 926
- Satyapal S., Vega D., Heckman T., O'Halloran B., Dudik R., 2007, *ApJ*, 663, L9
- Schawinski K., Thomas D., Sarzi M., Maraston C., Kaviraj S., Joo S.-J., Yi S. K., Silk J., 2007, *MNRAS*, 382, 1415
- Schödel R., Ott T., Genzel R., Eckart A., Mouawad N., Alexander T., 2003, *ApJ*, 596, 1015
- Schramm M. et al., 2013, *ApJ*, 773, 150
- Shields J. C., 1992, *ApJ*, 399, L27
- Shirazi M., Brinchmann J., 2012, *MNRAS*, 421, 1043
- Stasińska G., Cid Fernandes R., Mateus A., Sodré L., Asari N. V., 2006, *MNRAS*, 371, 972
- Stern D. et al., 2012, *ApJ*, 753, 30
- Stern D. et al., 2005, *ApJ*, 631, 163
- Taniguchi Y., Shioya Y., Murayama T., 2000, *AJ*, 120, 1265
- Terlevich R., Melnick J., Masegosa J., Moles M., Copetti M. V. F., 1991, *A&AS*, 91, 285
- Tremaine S. et al., 2002, *ApJ*, 574, 740
- Trouille L., Barger A., Tremonti C., 2011, in *Bulletin of the American Astronomical Society*, Vol. 43, American Astronomical Society Meeting Abstracts #217, p. #326.03
- Urry C. M., Padovani P., 1995, *PASP*, 107, 803
- Veilleux S., Osterbrock D. E., 1987, *ApJS*, 63, 295
- Volonteri M., 2010, *A&A Rev.*, 18, 279
- Volonteri M., Lodato G., Natarajan P., 2008, *MNRAS*, 383, 1079
- Wright E. L. et al., 2010, *AJ*, 140, 1868
- Yun M. S., Reddy N. A., Condon J. J., 2001, *ApJ*, 554, 803

APPENDIX A: AGN CANDIDATES

Tables A1 – A7 give an overview of the AGN candidate samples. In the first column we list the object IDs used in this work. Stellar masses are given in solar masses M_{\odot} . The [O III] luminosity is given in erg/s. The last four columns show by which selection criteria the sources are classified as AGN.

APPENDIX B: HOST GALAXY PROPERTIES

In Section 4 we analysed different host galaxy properties separately. However, most of these parameters are correlated with each other, and a simple histogram comparison can be highly misleading. For this reason Figures B1, B2 and B3 show the 2D relations of some of these quantities. In all the cases the BPT and He II selected AGN samples seem to separate on the 2D planes from most of the mid-IR sample. This suggests that mid-IR selection and optical selection are revealing two different classes of AGN host galaxies.

This paper has been typeset from a $\text{\TeX}/\text{\LaTeX}$ file prepared by the author.

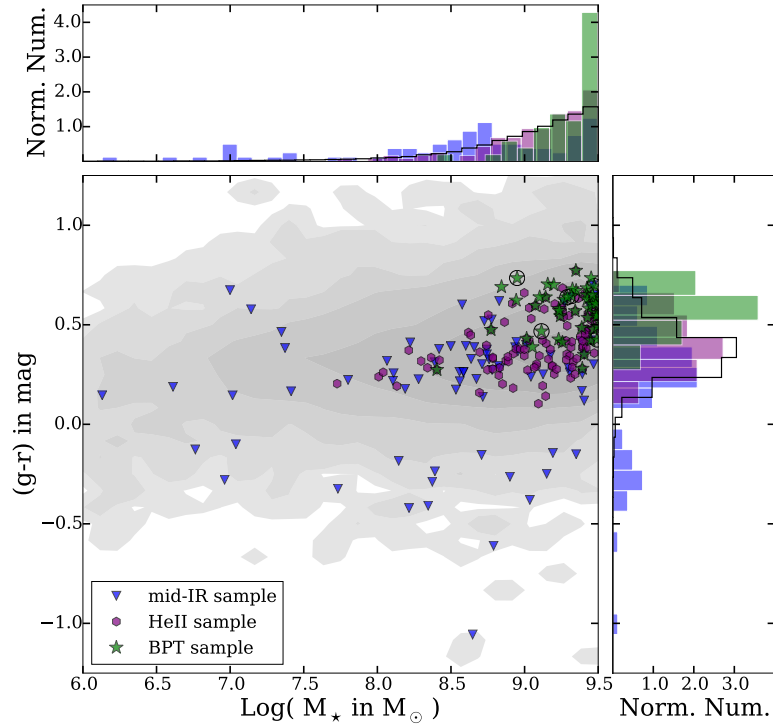


Figure B1. $(g-r)$ versus stellar mass distribution for the parent sample (gray shaded area) and the AGN candidates. Green stars refer to AGN candidates selected with BPT diagram (the circled stars show the AGN candidates with upper limits for the $H\beta$ flux), purple hexagons to He II selected AGN candidates, and blue triangles to mid-IR selected candidates. Only objects with r -band magnitude $r < 17.77$ are considered. The histograms are the same as shown in Fig. 6 - 8. The three samples of AGN candidates seem to separate on the 2D plane. In particular, mid-IR selected AGN candidates are bluer compared to the optically selected ones (BPT and He II selection). He II selected AGN candidates are bluer compared to the BPT sample, but still redder than the mid-IR sample.

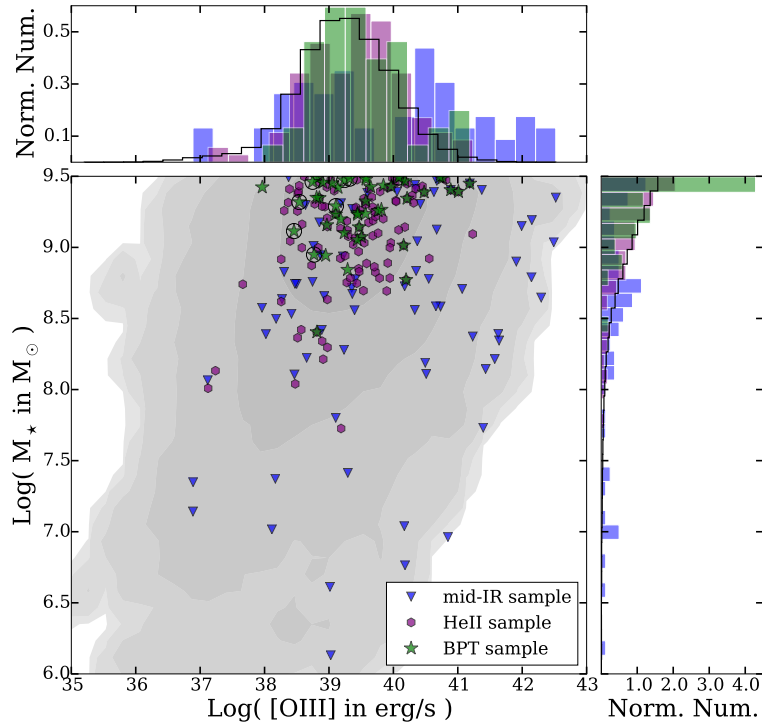


Figure B2. Same as Fig. B1 but for the mass versus $[O\text{ III}]\lambda 5007$ distribution. Optically selected AGN candidates are found only at high masses compared to the mid-IR selected ones, and the $[O\text{ III}]$ luminosity is slightly lower.

ID	RA	DEC	MJD_Plate_Fiber	redshift	Log M_*	L [O III]	BPT	HeII	Mid-IR Stern	Mid-IR Jarrett
5424 ^{b,c}	12:07:46.11	+43:07:34.9	53120_1450_353	0.0031	9.35	38.85	✓	✓		
6868 ^{b,c}	09:49:41.20	+32:13:16.0	53432_1946_536	0.0051	9.23	39.10	✓	✓		
7382 ^{b,c}	14:48:42.57	+12:27:26.0	53521_1714_376	0.0060	9.49	38.81	✓			
7489 ^{b,c}	16:23:35.08	+45:44:43.5	52377_624_111	0.0062	9.42	37.96	✓			
7802 ^{b,c}	11:09:12.39	+61:23:46.7	52295_775_309	0.0067	8.40	38.81	✓	✓		
11779 ^{a,b}	10:09:35.66	+26:56:49.0	53757_2347_456	0.0143	8.77	40.20	✓	✓		
12254 ^a	08:40:25.55	+18:18:59.0	53711_2278_445	0.0150	9.14	39.47	✓	✓		
12776	14:31:46.76	+26:16:24.4	53827_2135_453	0.0156	9.35	38.81	✓			
12974 ^{a,b}	08:11:45.30	+23:28:25.7	52943_1584_567	0.0158	9.07	39.50	✓	✓		
14523 ^{a,b,c}	14:05:10.40	+11:46:16.9	53799_1703_510	0.0175	9.24	39.44	✓	✓		
14807	00:21:45.81	+00:33:27.3	51900_390_465	0.0177	9.16	38.97	✓			
16257 ^a	14:02:28.73	+09:18:56.4	54175_1807_560	0.0192	8.84	39.29	✓			
20566 ^c	12:11:53.18	+23:38:37.3	54210_2644_561	0.0220	9.50	40.11	✓	✓		
22827 ^{a,c}	13:04:57.86	+36:26:22.2	53799_2016_414	0.0229	9.23	39.45	✓			
23389 ^a	11:43:02.41	+26:08:19.0	53792_2221_218	0.0231	9.27	39.81	✓			
27247 ^a	11:05:03.96	+22:41:23.5	54149_2488_561	0.0248	9.10	39.24	✓			
27843 ^a	02:48:25.27	-00:25:41.4	51871_409_150	0.0251	8.94	38.95	✓			
31578 ^a	11:13:19.24	+04:44:25.2	52326_835_433	0.0267	9.24	39.57	✓			
33647	09:07:37.06	+35:28:28.4	52703_1212_97	0.0275	9.44	39.85	✓			
37125	08:42:34.51	+03:19:30.7	52224_564_422	0.0288	9.34	40.21	✓	✓		
38791	17:32:02.97	+59:58:54.8	51792_354_2	0.0293	9.05	39.44	✓			
39324 ^a	08:42:04.93	+40:39:34.5	52296_829_391	0.0295	9.20	39.18	✓			
40089 ^a	14:40:12.70	+02:47:43.5	52024_536_575	0.0298	9.45	41.19	✓	✓	✓	
40160 ^a	09:02:22.76	+14:10:49.2	53820_2433_569	0.0298	9.42	39.14	✓			
43170 ^a	14:20:44.95	+22:42:36.9	54540_2786_552	0.0308	9.49	39.58	✓			
45285 ^a	09:21:29.99	+21:31:39.4	53727_2290_185	0.0315	9.43	39.65	✓			
45874	16:09:43.05	+26:47:41.8	52824_1393_505	0.0317	9.45	39.05	✓			
48664 ^a	09:54:18.16	+47:17:25.1	54525_2956_457	0.0326	9.49	40.76	✓	✓	✓	✓
48794 ^a	14:12:08.47	+10:29:53.9	53848_1705_98	0.0326	9.01	40.16	✓	✓		
48830 ^a	11:44:18.84	+33:40:07.5	53491_2097_228	0.0326	9.33	39.57	✓			
49040	01:19:05.14	+00:37:45.1	51789_398_585	0.0327	9.26	39.76	✓			
49415	13:17:51.36	+53:06:44.9	52722_1040_41	0.0328	9.46	38.90	✓			
59191	00:42:14.99	-10:44:15.0	52162_655_59	0.0359	9.47	40.18	✓	✓		
74272 ^a	13:49:39.37	+42:02:41.4	52814_1345_41	0.0412	9.39	40.48	✓	✓		
78416	09:44:51.02	+12:30:44.1	53053_1742_451	0.0426	9.48	39.57	✓			
84989 ^c	13:47:36.40	+17:34:04.6	54233_2742_442	0.0447	9.39	41.01	✓	✓		
87145	10:44:24.58	+18:40:09.4	54174_2479_461	0.0453	9.43	39.29	✓			
89308 ^a	15:39:41.68	+17:14:21.9	54563_2795_509	0.0459	9.50	40.72	✓	✓		
92048 ^a	09:06:13.77	+56:10:15.2	51908_450_409	0.0466	9.40	40.89	✓	✓	✓	✓
97445 ^a	13:04:34.92	+7:55:05.1	54504_1794_547	0.0482	9.43	39.96	✓	✓		
17389*	11:48:47.66	+20:10:00.5	54180_2515_357	0.0202	9.32	38.54	✓			
19871*	11:42:03.18	+16:46:34.4	53875_2508_197	0.0216	8.95	38.77	✓			
38107*	03:04:51.42	+00:12:18.2	51817_411_553	0.0291	9.29	39.11	✓			
59007*	13:13:05.86	+23:27:33.7	54507_2651_405	0.0359	9.47	39.24	✓			
64110*	13:41:56.15	+50:06:42.2	53433_1669_168	0.0376	9.11	38.46	✓			
73934*	08:30:23.50	+38:55:54.2	52615_894_20	0.0411	9.48	39.32	✓			
74705*	14:32:35.92	+14:35:21.8	54233_2747_113	0.0414	9.46	38.75	✓			
100261*	02:33:46.94	-01:01:28.3	51820_407_6	0.0491	9.49	40.08	✓			

Table A1. BPT selected AGN candidates - 1/1. In the first column we list the object IDs used in this work. Stellar masses are given in solar masses M_{\odot} . The [O III] luminosity is given in erg/s. For the objects labeled with * we assumed upper limits for $H\beta$. The last four columns show by which selection criteria the sources are classified as AGN.

^a Classified as AGN also in Reines, Greene & Geha (2013)

^b Classified as AGN also in Moran et al. (2014)

^c Extended flag in WISE

ID	RA	DEC	MJD_Plate_Fiber	redshift	Log M_{\star}	L [O III]	BPT	HeII	Mid-IR Stern	Mid-IR Jarrett
5041 ^c	01:42:26.99	+13:58:37.1	51820_429_352	0.0025	8.01	37.12		✓		
5424 ^{b,c}	12:07:46.11	+43:07:34.9	53120_1450_353	0.0031	9.35	38.85	✓	✓		
5426 ^{b,c}	11:51:13.43	+50:09:24.8	52412_968_386	0.0031	9.26	38.30		✓		
5634 ^c	12:08:42.33	+36:48:10.0	53472_2105_348	0.0034	8.13	37.24		✓		
6868 ^{b,c}	09:49:41.20	+32:13:16.0	53432_1946_536	0.0051	9.23	39.10	✓	✓		
7106 ^c	14:58:46.08	+02:58:08.6	52055_589_282	0.0055	8.21	38.91		✓		
7192 ^c	10:38:01.62	+64:15:58.9	51930_489_50	0.0057	9.13	39.18		✓		
7265 ^c	16:06:41.00	+06:34:51.4	53858_1729_120	0.0058	8.42	38.57		✓		
7775 ^{b,c}	12:25:05.61	+05:19:44.8	54509_2880_503	0.0067	9.00	38.58		✓		
7777 ^c	11:14:37.21	+30:18:50.9	53460_2092_1	0.0067	9.41	38.39		✓		
7802 ^{b,c}	11:09:12.39	+61:23:46.7	52295_775_309	0.0067	8.40	38.81	✓	✓		
8012	08:26:04.39	+45:58:03.5	51981_549_291	0.0071	9.16	38.58		✓		
8021 ^c	12:53:59.23	+29:47:19.1	53726_2239_38	0.0071	8.04	38.48		✓		
8217 ^c	08:27:27.68	+25:43:27.9	52945_1586_146	0.0075	8.62	38.26		✓		
8588 ^{b,c}	13:51:25.37	+40:12:47.8	53061_1378_388	0.0082	9.03	39.96		✓		
8807 ^c	08:12:56.37	+54:58:08.4	53383_1782_345	0.0086	9.32	38.37		✓		
9175 ^c	03:00:40.20	+00:01:13.3	51817_411_270	0.0095	8.74	37.66		✓		
9250 ^c	09:58:47.13	+11:23:19.3	53055_1744_289	0.0097	9.04	38.40		✓		
9533 ^{b,c}	09:48:00.79	+09:58:15.4	52996_1306_274	0.0104	8.75	39.28		✓		
9690 ^c	11:18:36.35	+63:16:50.3	52370_596_10	0.0107	9.32	39.56		✓		
9874 ^c	22:10:20.63	-09:11:31.4	52206_718_140	0.0110	8.36	38.51		✓		
10219	00:31:27.55	-10:40:33.2	52146_654_219	0.0117	7.73	39.19		✓		
11212 ^c	13:40:36.28	+34:17:38.2	53818_2028_312	0.0136	9.00	38.83		✓		
11779 ^{a,b}	10:09:35.66	+26:56:49.0	53757_2347_456	0.0143	8.77	40.20	✓	✓		
12254 ^{a,b}	08:40:25.55	+18:18:59.0	53711_2278_445	0.0150	9.14	39.47	✓	✓		
12269	15:23:07.79	+19:05:01.4	54328_2159_201	0.0150	8.63	38.97		✓		
12840 ^c	13:19:49.95	+52:03:41.2	53430_1667_510	0.0156	8.85	39.46		✓		
12974 ^{a,b}	08:11:45.30	+23:28:25.7	52943_1584_567	0.0158	9.07	39.50	✓	✓		
13986	13:57:50.41	+26:42:40.7	53852_2120_293	0.0169	8.78	39.33		✓		
14523 ^{a,b,c}	14:05:10.40	+11:46:16.9	53799_1703_510	0.0175	9.24	39.44	✓	✓		
15541 ^c	11:42:53.93	+00:09:42.8	51959_283_426	0.0184	9.19	39.28		✓		
15565	12:27:57.72	+54:30:47.6	52707_1019_36	0.0185	8.30	38.98		✓		
16383 ^c	12:03:03.59	+56:55:00.3	53050_1314_272	0.0193	9.45	40.03		✓		
17149	09:39:50.23	+36:10:27.9	52992_1594_404	0.0200	8.70	39.53		✓		
18265 ^c	12:13:45.77	+24:21:21.8	54484_2656_21	0.0208	9.50	38.62		✓		
18643 ^c	11:06:28.99	+44:51:03.3	53054_1436_8	0.0210	9.48	39.44		✓		
20161	12:06:22.54	+31:56:29.1	53474_2095_65	0.0218	8.83	39.72		✓		
20271	13:14:37.66	+29:19:04.9	53904_2009_621	0.0218	9.26	39.48		✓		
20566 ^c	12:11:53.18	+23:38:37.3	54210_2644_561	0.0220	9.50	40.11	✓	✓		
20955	09:04:27.03	+29:18:56.0	53357_1934_620	0.0221	8.83	39.47		✓		
22633	11:24:51.32	+29:28:48.0	53794_2217_430	0.0228	9.03	39.55		✓		
25147	11:10:23.98	+60:51:51.8	52286_774_116	0.0238	9.17	39.61		✓		
25780	09:44:46.54	+13:32:23.6	54139_2582_251	0.0241	8.75	39.43		✓		
26813	12:26:03.64	+08:15:19.0	53472_1626_541	0.0246	9.30	39.57		✓		
26925	12:05:50.50	+15:54:46.4	53467_1764_527	0.0246	8.34	38.89		✓		
27867	14:03:11.15	+30:51:59.5	54180_2121_86	0.0251	9.15	38.98		✓		
28192 ^c	07:55:14.82	+53:44:43.7	53383_1870_336	0.0252	9.29	38.94		✓		
28437	14:13:26.76	+02:25:09.3	51994_533_396	0.0253	8.57	39.16		✓		
28650 ^c	12:30:26.35	+10:30:59.8	52731_1232_471	0.0254	9.42	38.97		✓		
29421	10:48:25.08	+38:21:10.2	53474_2007_376	0.0257	8.92	38.26		✓		
29439	09:20:04.27	-00:30:08.9	52000_474_313	0.0257	8.86	39.70		✓		
30515	11:17:45.95	+25:33:32.1	53794_2214_14	0.0262	9.26	38.51		✓		
30891 ^c	11:46:22.21	+49:53:21.4	52636_967_583	0.0264	9.31	38.78		✓		
33190	11:01:47.95	+09:53:50.4	52723_1220_559	0.0273	9.21	38.97		✓		
34084 ^a	13:47:57.68	+46:54:35.0	52736_1284_95	0.0277	9.36	40.29		✓		
35611	09:21:49.44	+23:34:38.7	53714_2291_88	0.0282	9.29	38.90		✓		
36713	11:10:36.82	+29:29:28.3	53793_2215_351	0.0286	8.78	39.79		✓		
37026	12:44:33.49	+31:05:05.8	53828_2237_607	0.0287	8.92	39.18		✓		
37125	08:42:34.51	+03:19:30.7	52224_564_422	0.0288	9.34	40.21	✓	✓		
37135	15:00:40.51	+11:56:47.4	53827_1716_474	0.0288	9.08	39.30		✓		

Table A2. He II selected AGN candidates - 1/2. In the first column we list the object IDs used in this work. Stellar masses are given in solar masses M_{\odot} . The [O III] luminosity is given in erg/s. The last four columns show by which selection criteria the sources are classified as AGN.

^a Classified as AGN also in Reines, Greene & Geha (2013), ^b Classified as AGN also in Moran et al. (2014)

^c Extended flag in WISE

ID	RA	DEC	MJD_Plate_Fiber	redshift	Log M _★	L [O III]	BPT	HeII	Mid-IR Stern	Mid-IR Jarrett
37577	13:46:55.01	+22:58:15.0	54230.2666_10	0.0289	9.26	38.09		✓		
37767	13:31:10.68	-01:57:01.3	52426.911_470	0.0290	9.38	38.52		✓		
37935	10:54:30.41	+57:22:09.7	52427.949_133	0.0290	8.94	39.25		✓		
38474	07:55:38.19	+24:01:03.6	52669.1204_474	0.0292	8.87	38.73		✓		
39909	03:26:14.06	-01:04:41.8	51901.414_240	0.0297	8.97	39.46		✓		
40089 ^a	14:40:12.70	+2:47:43.5	52024.536_575	0.0298	9.45	41.19	✓	✓	✓	
40922	10:52:40.65	+19:56:41.3	54175.2482_404	0.0301	9.39	38.53		✓		
42593	16:43:25.94	+39:19:52.0	52395.818_556	0.0306	9.20	39.84		✓		
43283	12:22:42.20	+51:14:49.2	52644.971_325	0.0308	9.40	39.08		✓		
43400	10:03:59.65	+41:29:04.6	52672.1217_108	0.0309	9.28	39.42		✓		
44006	09:15:23.86	+6:23:02.0	52652.1193_564	0.0311	8.72	39.75		✓		
45715	17:16:50.09	+57:04:55.5	51788.355_160	0.0316	9.47	39.03		✓		
47952	11:33:27.78	+45:51:32.1	53050.1442_97	0.0323	9.02	39.37		✓		
48274	16:20:01.08	+08:22:58.6	54585.2529_69	0.0324	9.43	38.54		✓		
48473	13:19:39.35	+26:47:16.9	53795.2244_352	0.0325	9.08	39.68		✓		
48664 ^a	09:54:18.16	+47:17:25.1	54525.2956_457	0.0326	9.49	40.76	✓	✓	✓	✓
48794 ^a	14:12:08.47	+10:29:53.9	53848.1705_98	0.0326	9.01	40.16	✓	✓		
51040	09:24:03.82	+29:07:01.4	53389.1939_265	0.0333	9.48	38.86		✓		
51329	15:12:45.01	+26:34:49.3	54242.2157_240	0.0334	8.79	39.72		✓		
51623	16:56:01.15	+19:48:38.3	53172.1567_361	0.0335	8.78	39.95		✓		
51844	11:25:54.17	+31:53:48.4	53431.1979_575	0.0336	8.89	39.91		✓		
52164	08:19:04.91	+17:34:23.7	53726.2271_239	0.0337	9.12	39.29		✓		
52742	10:10:19.10	+29:08:05.8	53757.2348_462	0.0338	9.10	39.76		✓		
53841	15:36:08.38	+25:27:03.8	53823.2163_618	0.0342	9.46	38.86		✓		
54785	14:33:46.88	+36:26:51.2	53115.1382_305	0.0345	9.45	40.21		✓		
57701	11:47:56.66	+9:05:41.8	52734.1226_138	0.0354	8.89	39.58		✓		
58986 ^c	13:10:41.07	+44:01:07.4	53084.1375_233	0.0359	9.43	40.45		✓		
59191	00:42:14.99	-10:44:15.0	52162.655_59	0.0359	9.47	40.18	✓	✓		
60982	16:16:47.19	+18:01:09.4	54585.2968_78	0.0366	9.28	39.68		✓		
63123	11:21:49.60	+11:54:08.1	53062.1605_105	0.0373	9.19	39.68		✓		
63673	13:01:43.44	+04:08:36.7	52439.849_212	0.0375	9.22	39.72		✓		
65042	14:04:00.01	+10:38:31.7	53799.1703_143	0.0379	9.39	39.79		✓		
65837	14:52:48.17	+23:46:18.6	53770.2144_615	0.0382	9.25	39.71		✓		
66137	15:26:37.36	+06:59:41.7	54540.1819_496	0.0383	9.41	40.35		✓		✓
67600	08:14:31.33	+08:12:50.1	54055.2571_306	0.0388	9.49	39.99		✓		
69278	14:48:31.55	+16:53:28.3	54554.2777_243	0.0395	9.33	40.04		✓		
69465	15:34:25.59	+04:08:06.7	52026.593_547	0.0395	9.38	39.57		✓		
71190	15:40:28.95	+34:33:40.0	52872.1402_182	0.0401	8.69	39.90		✓		
73703	08:51:25.82	+39:35:41.7	52669.1198_392	0.0410	9.31	40.31		✓		
74024	09:51:18.31	+39:41:54.4	52765.1277_361	0.0411	9.00	39.95		✓		
74272 ^a	13:49:39.37	+42:02:41.4	52814.1345_41	0.0412	9.39	40.48	✓	✓		
75308	11:49:39.99	+36:57:28.7	53436.2035_411	0.0416	9.14	40.18		✓		
78715	14:42:52.78	+20:54:51.7	54555.2789_485	0.0427	8.92	40.56		✓		
82176	10:21:17.14	+15:05:24.2	54175.2590_206	0.0438	9.32	40.04		✓		
84207	11:04:44.71	+63:16:42.5	52370.596_290	0.0444	9.07	39.40		✓		
84592	14:42:32.70	+21:24:02.1	54555.2789_460	0.0445	9.41	39.62		✓		
84989 ^c	13:47:36.40	+17:34:04.6	54233.2742_442	0.0447	9.39	41.01	✓	✓		
86119	01:56:45.30	-00:37:37.8	51871.403_186	0.0450	9.42	39.91		✓		
89308 ^a	15:39:41.68	+17:14:21.9	54563.2795_509	0.0459	9.50	40.72	✓	✓		
92048 ^a	09:06:13.77	+56:10:15.2	51908.450_409	0.0466	9.40	40.89	✓	✓	✓	✓
97445 ^a	13:04:34.92	+07:55:05.1	54504.1794_547	0.0482	9.43	39.96	✓	✓		
99464	16:24:35.17	+47:32:15.8	52377.624_597	0.0488	9.12	40.08		✓		
101460	10:41:19.81	+14:36:41.2	53112.1748_609	0.0494	9.49	41.03		✓		
101985	13:50:42.06	+17:04:46.7	54233.2742_563	0.0496	9.35	39.67		✓		
108738	01:00:05.94	-01:10:59.0	51783.395_58	0.0515	9.47	40.82		✓		
112045	14:03:46.96	+33:10:10.2	54180.2121_460	0.0523	9.34	39.54		✓		
114145 ^a	15:40:59.61	+31:55:07.3	53149.1581_255	0.0528	9.09	41.23		✓		
120037	09:43:45.20	+01:30:57.5	51989.480_264	0.0543	9.39	39.50		✓		
129072	00:58:18.14	-08:44:15.7	52146.658_365	0.0569	9.39	39.67		✓		
130041	11:14:28.35	+01:44:04.3	52381.510_137	0.0571	9.43	39.53		✓		
160721	00:24:09.49	-01:00:32.3	51900.390_17	0.0645	9.36	39.54		✓		

Table A3. HeII selected AGN candidates - 2/2. In the first column we list the object IDs used in this work. Stellar masses are given in solar masses M_☉. The [O III] luminosity is given in erg/s. The last four columns show by which selection criteria the sources are classified as AGN.

^a Classified as AGN also in Reines, Greene & Geha (2013)

^c Extended flag in WISE

ID	RA	DEC	MJD_Plate.Fiber	redshift	Log M_{\star}	L [O III]	BPT	HeII	Mid-IR Stern	Mid-IR Jarrett
5449	12:19:23.35	+19:35:14.4	54477_2611_266	0.0032	7.00	-			✓	
5619	12:01:22.31	+02:11:08.3	52017_516_178	0.0034	6.13	39.03			✓	
6642	02:53:28.64	-08:59:05.5	51901_457_213	0.0049	7.14	36.89			✓	✓
6689	11:51:04.82	+05:14:46.4	52373_839_623	0.0049	6.61	39.02			✓	
7289	15:01:00.85	+01:00:49.9	52017_539_205	0.0058	7.35	36.89			✓	
7629	12:46:10.75	+26:15:00.8	54205_2238_135	0.0064	7.41	39.29			✓	
7969	08:44:42.71	+29:32:43.1	52937_1269_18	0.0070	7.29	37.77			✓	
9030	16:47:10.66	+21:05:14.5	53149_1570_21	0.0091	6.76	40.18			✓	✓
9612	08:42:36.58	+10:33:13.9	54061_2573_493	0.0105	7.04	40.17			✓	
10763	02:18:52.90	-09:12:18.7	52162_668_152	0.0128	7.07	40.27			✓	✓
10897	11:29:25.96	+21:21:07.6	54178_2500_180	0.0131	7.80	39.10			✓	
10957	10:44:57.80	+03:53:13.1	52339_578_60	0.0132	6.96	40.85			✓	
11102	08:01:23.72	+39:53:22.5	52201_544_524	0.0134	8.83	38.30			✓	
11105	08:22:40.29	+03:45:46.6	52642_1185_235	0.0134	8.50	38.18			✓	✓
11826	09:31:56.90	+42:48:58.0	52670_940_332	0.0144	8.11	40.51			✓	
12643	08:02:22.88	+23:24:28.9	52705_1265_306	0.0154	7.98	38.37			✓	
12868	13:29:32.42	+32:34:17.1	53534_2112_35	0.0157	8.11	38.46			✓	✓
14176	11:55:28.34	+57:39:51.9	52790_1313_423	0.0171	7.73	41.39			✓	
14294	09:25:24.54	+02:03:49.3	51965_475_359	0.0173	8.22	38.65			✓	
14926	00:59:04.10	+01:00:04.3	51783_395_525	0.0178	8.83	40.35			✓	✓
15020	12:23:16.53	+04:50:10.1	54509_2880_230	0.0179	8.71	41.07			✓	
15156	11:36:51.14	+07:40:25.2	53084_1619_549	0.0181	8.72	39.35			✓	
15175	08:48:20.17	+26:24:49.9	53350_1932_188	0.0181	8.42	38.89			✓	
17350	09:47:22.14	+00:44:26.9	51630_266_616	0.0201	9.31	39.19			✓	
17373	08:38:01.53	+18:43:12.4	53705_2277_216	0.0202	8.58	37.96			✓	
17394	07:56:42.18	+35:36:33.0	52238_757_177	0.0202	8.39	37.52			✓	
18167	08:24:47.50	+18:32:43.7	53709_2273_446	0.0208	8.29	39.11			✓	
19109	09:15:05.13	+28:56:41.0	53330_1936_27	0.0213	8.39	38.02			✓	
20311	09:16:40.98	+18:28:07.9	53795_2439_372	0.0218	7.45	40.91			✓	
20747	23:53:52.51	-00:05:55.4	51788_386_154	0.0220	9.47	38.12			✓	
20756 ^c	13:38:15.38	-00:23:54.8	51671_299_222	0.0220	9.04	40.37			✓	✓
21077	11:56:35.19	+27:39:42.2	53819_2226_381	0.0222	8.32	38.93			✓	
22237	11:07:36.72	+05:33:37.6	52356_581_443	0.0227	8.64	38.27			✓	
22729	12:10:08.35	+44:39:06.6	53089_1369_15	0.0229	7.27	40.61			✓	
22732	13:28:52.96	+15:59:34.3	54154_2606_231	0.0229	7.21	40.95			✓	
23130	13:41:41.61	+35:02:14.1	53818_2028_390	0.0230	8.73	40.17			✓	
23535	12:10:32.56	+44:36:04.5	53090_1370_247	0.0232	8.19	40.49			✓	
24664	13:12:06.27	+5:10:59.7	52338_850_504	0.0236	8.37	39.14			✓	
24892	10:29:43.29	+20:25:54.3	53770_2376_360	0.0237	8.78	39.41			✓	
25946	23:03:03.22	-08:25:06.3	52258_725_447	0.0242	8.17	38.90			✓	
29484	22:39:31.32	-00:40:36.2	52145_377_152	0.0257	6.96	38.63			✓	
30698	16:46:15.62	+43:54:54.3	52051_629_104	0.0263	8.27	39.90			✓	
33249	09:14:36.22	+18:16:02.5	53848_2437_572	0.0273	8.79	38.27			✓	
35203	10:54:21.65	+2:11:36.5	52353_507_120	0.0281	8.71	-			✓	
35452	11:45:40.24	-00:34:15.0	51959_283_164	0.0282	8.56	40.33			✓	
38058	07:58:24.06	+17:07:45.7	53317_1921_638	0.0291	8.53	38.42			✓	
38410	10:18:57.31	+06:25:23.1	52750_998_307	0.0292	8.77	37.46			✓	
39895	12:48:13.45	+43:57:03.5	53063_1373_218	0.0297	8.78	40.55			✓	
40089 ^a	14:40:12.70	+02:47:43.5	52024_536_575	0.0298	9.45	41.19	✓	✓	✓	
42470	16:01:35.96	+31:13:53.8	52826_1405_395	0.0306	8.58	40.73			✓	✓
43060	08:28:58.96	+08:48:31.8	53084_1758_452	0.0308	8.56	39.40			✓	✓
44058	08:45:27.61	+53:08:52.9	51877_447_361	0.0311	8.14	41.43			✓	
45052	15:47:48.99	+22:03:03.2	53556_2169_41	0.0314	7.80	41.26			✓	
48098	10:56:08.75	+24:09:26.0	53876_2486_363	0.0324	8.94	39.22			✓	
48664 ^a	09:54:18.16	+47:17:25.1	54525_2956_457	0.0326	9.49	40.76	✓	✓	✓	✓
48849	15:09:34.17	+37:31:46.1	53172_1399_299	0.0326	7.86	41.66			✓	
49838	14:23:42.87	+22:57:28.8	53493_2132_241	0.0329	7.72	41.35			✓	
50820	11:32:57.32	+31:28:31.9	53430_1974_155	0.0333	7.59	40.93			✓	
52246	09:58:50.00	+67:27:08.8	54478_1879_88	0.0337	9.44	40.34			✓	

Table A4. Mid-IR selected AGN candidates - 1/4ss. In the first column we list the object IDs used in this work. Stellar masses are given in solar masses M_{\odot} . The [O III] luminosity is given in erg/s. The last four columns show by which selection criteria the sources are classified as AGN.

^a Classified as AGN also in Reines, Greene & Geha (2013)

^c Extended flag in WISE

ID	RA	DEC	MJD_Plate_Fiber	redshift	Log M_{\star}	L [O III]	BPT	HeII	Mid-IR Stern	Mid-IR Jarrett
54437	16:21:52.57	+15:18:56.0	53880_2208_306	0.0344	8.39	41.63			✓	
59304	13:03:54.44	+37:14:01.9	53800_2018_96	0.0360	8.35	41.64			✓	
60324	14:16:15.62	-01:27:52.7	52400_917_336	0.0363	8.37	41.23			✓	
64919	15:45:43.55	+08:58:01.3	54266_1725_68	0.0379	8.18	41.96			✓	
66259	08:58:06.35	+49:49:47.5	51993_551_76	0.0384	9.01	38.76			✓	
68371	09:05:31.08	+03:35:30.4	52238_566_497	0.0391	8.08	41.34			✓	✓
71440	16:19:23.61	+25:40:10.1	53496_1576_136	0.0402	8.82	38.34			✓	
72486	16:39:37.27	+27:07:50.2	54553_2948_20	0.0406	7.61	40.58			✓	
74640	14:18:43.41	+28:09:57.5	53881_2130_238	0.0414	8.40	41.36			✓	
85569	09:40:00.52	+20:31:22.5	53762_2361_523	0.0448	8.35	41.34			✓	
86653	10:20:11.34	+01:30:46.0	51999_503_126	0.0451	9.10	38.71			✓	
86812	15:56:16.29	+08:59:17.3	53137_1726_627	0.0452	9.38	39.60			✓	✓
88704	10:23:52.66	+41:52:11.0	53002_1359_412	0.0457	9.01	39.07			✓	
91423	15:03:10.43	+18:43:08.8	54556_2792_284	0.0464	8.78	40.76			✓	✓
92048 ^a	09:06:13.77	+56:10:15.2	51908_450_409	0.0466	9.40	40.89	✓	✓	✓	✓
94970	17:35:01.25	+57:03:08.6	51818_358_504	0.0474	8.65	42.29			✓	✓
95418	09:58:59.36	+55:24:15.8	52652_945_423	0.0475	8.33	41.06			✓	✓
99925	12:28:22.82	+20:20:43.6	54477_2611_634	0.0489	8.08	41.12			✓	✓
105680	09:02:50.25	+14:14:10.1	53826_2434_411	0.0506	9.31	40.42			✓	✓
105787	10:39:30.40	+14:19:13.2	53112_1748_526	0.0507	8.54	40.76			✓	✓
111723	13:12:53.77	+17:12:31.2	54484_2604_439	0.0522	8.20	41.37			✓	✓
112658	08:41:39.50	+21:34:53.3	53360_2084_12	0.0525	9.37	39.40			✓	
115666	15:12:12.85	+47:16:30.7	52721_1050_402	0.0532	9.15	41.99			✓	
122293	10:45:20.42	+09:23:49.1	53491_2147_514	0.0549	8.90	41.91			✓	
123356	15:53:20.20	+42:07:35.7	52764_1334_271	0.0552	8.60	-			✓	✓
123713	10:47:38.17	+04:18:41.8	52339_578_32	0.0553	8.51	41.08			✓	
128255	13:35:48.08	+37:01:45.7	53858_2101_387	0.0566	8.48	41.66			✓	
128455	14:15:49.61	+01:37:56.5	51994_533_172	0.0567	8.42	40.87			✓	✓
128605	01:47:07.06	+13:56:29.1	51820_429_495	0.0567	8.45	41.80			✓	
132736	14:45:36.16	+63:40:46.2	52339_609_376	0.0580	9.18	40.99			✓	
134273	10:32:06.02	+22:59:21.8	53763_2367_475	0.0585	8.89	40.92			✓	✓
137290	08:47:02.08	+03:52:02.0	52650_1188_7	0.0593	9.47	40.67			✓	
137647	00:49:59.83	-00:24:15.8	51913_394_269	0.0595	8.76	40.67			✓	
141121	13:03:03.32	+35:51:28.6	53799_2016_394	0.0603	8.77	41.93			✓	
145508	10:10:42.54	+12:55:16.8	53061_1745_475	0.0614	8.79	42.14			✓	✓
154841	14:51:55.51	+22:51:57.7	53770_2144_550	0.0633	8.31	41.36			✓	✓
158388	12:39:08.59	+09:07:17.1	52734_1233_55	0.0640	9.42	39.80			✓	✓
160488	15:28:17.18	+39:56:50.5	52765_1293_580	0.0645	8.80	41.78			✓	
164973	08:56:33.04	+32:59:57.7	52974_1271_459	0.0654	9.17	40.38			✓	
164982	09:05:28.09	+44:10:58.3	52294_831_526	0.0654	8.74	41.91			✓	
166401	14:10:59.22	+43:02:46.9	53108_1394_294	0.0657	8.50	41.92			✓	
168543	23:29:36.55	-01:10:57.0	51821_384_281	0.0661	8.81	41.77			✓	✓
170095	12:36:13.64	+09:29:03.2	52734_1233_221	0.0664	8.88	40.94			✓	
171809	22:25:10.13	-00:11:52.9	52140_375_118	0.0668	8.45	42.00			✓	
176273	22:59:06.70	-00:58:10.0	51792_380_253	0.0677	9.22	41.49			✓	
178309	12:28:08.06	+07:54:43.4	53473_1627_426	0.0681	9.27	41.67			✓	
183496	10:13:34.35	+17:52:03.1	54138_2587_565	0.0692	9.40	41.37			✓	✓
189172	13:58:57.03	+13:38:59.7	53883_1778_74	0.0703	9.35	40.79			✓	✓
190553	13:44:27.36	+56:01:29.7	52791_1322_470	0.0706	9.19	42.15			✓	
197748	08:48:44.51	+51:06:26.7	51877_447_92	0.0719	8.71	41.35			✓	
199402	11:09:22.95	+14:56:37.1	53377_1751_579	0.0721	9.17	40.73			✓	✓
200366	08:40:00.37	+18:05:31.0	53711_2278_411	0.0723	8.31	41.92			✓	✓
204802	10:23:19.56	+02:49:41.5	51999_503_619	0.0731	9.12	41.07			✓	
208070	00:06:57.02	+00:51:26.0	51793_388_457	0.0737	8.63	41.89			✓	
208643	14:09:53.64	+29:32:37.4	53794_2126_427	0.0738	9.39	40.63			✓	✓
210237	11:43:48.30	+32:42:57.9	53473_2008_505	0.0740	8.60	42.05			✓	
211304	07:49:47.01	+15:40:13.3	53317_1921_281	0.0742	8.85	41.52			✓	
214163	09:06:28.49	+44:58:54.5	52606_898_45	0.0747	8.83	41.86			✓	
214566	04:09:37.63	-05:18:05.8	51910_465_524	0.0748	8.54	41.70			✓	

Table A5. Mid-IR selected AGN candidates - 2/4. In the first column we list the object IDs used in this work. Stellar masses are given in solar masses M_{\odot} . The [O III] luminosity is given in erg/s. The last four columns show by which selection criteria the sources are classified as AGN.

^a Classified as AGN also in Reines, Greene & Geha (2013)

ID	RA	DEC	MJD_Plate.Fiber	redshift	Log M_{\star}	L [O III]	BPT	HeII	Mid-IR Stern	Mid-IR Jarrett
216779	15:18:11.87	+19:55:14.5	54525_2156_81	0.0751	8.93	41.90			✓	
217992	14:55:33.68	+00:36:57.3	51994_309_489	0.0753	9.13	41.41			✓	✓
221600	08:52:21.72	+12:16:51.7	53815_2430_117	0.0760	9.04	42.49			✓	
226725	14:27:22.30	+03:25:08.1	52027_585_255	0.0768	9.12	41.53			✓	✓
230467	14:09:56.77	+54:56:48.9	52762_1325_412	0.0774	9.03	42.34			✓	
235966	09:28:10.52	+15:02:27.9	54068_2579_388	0.0784	9.21	41.78			✓	
237488	09:36:25.35	+05:03:32.2	52644_992_19	0.0786	8.69	41.84			✓	
240795	11:48:40.87	+17:56:33.0	53875_2508_615	0.0792	8.65	42.22			✓	
245310	11:52:15.03	+06:03:43.5	52374_840_446	0.0800	8.95	40.88			✓	
245739	00:34:13.95	-08:58:38.5	52146_654_563	0.0800	8.82	40.97			✓	
247612	11:13:20.52	+00:50:29.5	51984_279_377	0.0803	8.85	40.74			✓	✓
247767	10:36:57.59	+46:56:37.9	52620_962_227	0.0804	9.02	41.81			✓	✓
257429	12:00:16.49	+27:19:59.0	53819_2226_157	0.0819	8.59	42.23			✓	
266505	12:35:23.87	+03:45:35.8	52381_845_1	0.0834	8.90	41.70			✓	✓
272498	11:28:31.33	+61:12:55.6	52295_775_29	0.0845	8.74	41.99			✓	
273004	10:50:32.51	+15:38:06.3	53852_2483_254	0.0845	8.70	42.44			✓	
282992	14:28:05.51	+36:27:10.4	53144_1644_564	0.0863	8.90	42.14			✓	
284918	02:00:51.60	-08:45:43.0	52149_666_492	0.0867	8.97	41.67			✓	✓
285950	08:25:20.11	+08:27:23.2	53084_1758_338	0.0869	9.00	41.74			✓	✓
296262	11:51:52.09	+01:06:06.1	51943_284_448	0.0889	9.17	41.41			✓	
298133	09:00:47.44	+57:42:55.2	51924_483_495	0.0893	9.24	41.75			✓	✓
303639	09:26:09.41	+12:44:49.8	54093_2578_198	0.0905	9.49	40.93			✓	
306717	08:44:14.22	+02:26:21.3	52224_564_216	0.0912	9.25	42.34			✓	
309597	10:15:26.39	+30:54:51.8	53358_1953_618	0.0918	9.06	41.95			✓	✓
310250	14:50:56.60	+48:37:26.5	52736_1048_424	0.0920	9.24	42.37			✓	
310490	08:51:15.65	+58:40:55.0	54439_1785_201	0.0920	8.70	42.22			✓	
319086	09:29:18.39	+00:28:13.2	52000_474_610	0.0939	8.63	41.98			✓	✓
320814	13:29:16.55	+17:00:20.9	54154_2606_474	0.0943	9.03	42.36			✓	✓
325033	01:32:58.54	-08:53:37.8	52147_662_466	0.0952	8.77	41.84			✓	
332236	16:55:14.88	+31:29:54.3	52791_1176_198	0.0968	9.05	41.53			✓	✓
336179	09:50:23.32	+00:42:29.3	51608_267_421	0.0977	8.85	42.21			✓	✓
337345	10:48:39.11	+18:58:47.6	54175_2482_389	0.0980	9.12	41.89			✓	
338999	00:21:01.03	+00:52:48.1	51900_390_445	0.0984	9.35	42.52			✓	✓
340982	12:38:03.75	+46:18:20.1	53089_1455_287	0.0989	9.09	42.16			✓	
345440	13:17:10.89	+02:56:19.8	52295_525_626	0.0999	8.97	42.00			✓	✓
5784	10:53:24.34	+16:47:35.4	53852_2483_466	0.0036	7.02	38.11			✓	✓
6801	08:52:33.75	+13:50:28.4	53815_2430_597	0.0050	7.37	38.17			✓	✓
8102	11:26:18.42	+39:01:28.7	53436_1996_189	0.0073	8.07	37.12			✓	✓
16073	00:50:28.97	-00:31:50.0	51913_394_229	0.0190	8.28	39.23			✓	✓
18330	12:45:07.28	+14:19:12.1	53502_1769_40	0.0208	8.22	38.43			✓	✓
20575	10:39:29.83	+12:29:32.3	53112_1748_44	0.0220	8.25	39.18			✓	✓
20968	07:56:41.82	+28:22:18.8	52317_859_440	0.0221	8.74	38.50			✓	✓
31951	23:01:47.70	-09:35:04.6	52258_725_271	0.0268	8.82	38.15			✓	✓
32833	11:08:44.78	+36:18:33.5	53466_2034_538	0.0272	8.74	38.47			✓	✓
37334	07:51:08.94	+22:44:27.3	52669_1203_605	0.0288	9.27	39.36			✓	✓
44317	16:03:01.67	+39:37:44.3	52761_1055_403	0.0312	8.76	38.75			✓	✓
44445	20:56:05.90	-06:36:21.6	52176_636_176	0.0312	8.59	40.66			✓	✓
45155	08:46:24.12	+54:09:15.5	51899_446_154	0.0314	8.95	38.25			✓	✓
46464	14:18:01.74	+21:51:21.2	54540_2786_178	0.0319	8.67	39.36			✓	✓
47798	10:28:01.15	+08:48:51.9	52760_1239_193	0.0323	8.67	39.66			✓	✓
50838	11:36:42.73	+26:43:37.7	53816_2219_157	0.0333	8.94	38.87			✓	✓
50950	10:24:29.25	+05:24:51.0	52319_575_521	0.0333	8.22	41.57			✓	✓
53767	15:49:27.97	+10:47:27.0	54584_2520_166	0.0342	9.49	38.37			✓	✓
57906	10:55:27.96	+11:08:27.0	53117_1602_152	0.0355	8.91	38.69			✓	✓
59305	16:21:31.69	+10:07:30.8	54572_2531_230	0.0360	9.18	38.85			✓	✓
63239	10:30:23.33	+28:20:59.0	53794_2353_526	0.0373	8.57	40.89			✓	✓
64962	12:50:39.19	+62:10:34.8	52320_782_227	0.0379	8.63	39.58			✓	✓
66137	15:26:37.36	+06:59:41.7	54540_1819_496	0.0383	9.41	40.35		✓	✓	✓
88228	08:36:35.48	+22:17:40.5	53349_1929_74	0.0456	8.49	40.68			✓	✓
90892	15:49:08.14	+10:30:33.5	54584_2520_161	0.0463	9.30	38.64			✓	✓

Table A6. Mid-IR selected AGN candidates - 3/4. In the first column we list the object IDs used in this work. Stellar masses are given in solar masses M_{\odot} . The [O III] luminosity is given in erg/s. The last four columns show by which selection criteria the sources are classified as AGN.

ID	RA	DEC	MJD_Plate_Fiber	redshift	Log M_*	L [O III]	BPT	HeII	Mid-IR Stern	Mid-IR Jarrett
94610	10:23:45.04	+14:46:04.8	54175_2590_120	0.0473	9.13	40.67				✓
100483	10:35:09.33	+09:45:16.7	52734_1240_340	0.0491	8.22	41.33				✓
117208	13:00:31.42	+06:27:48.3	54504_1794_245	0.0536	9.36	38.72				✓
118838	11:20:40.48	+67:46:44.0	51942_491_456	0.0540	8.48	40.93				✓
129926	13:29:50.30	+31:11:14.2	53467_2110_466	0.0571	8.35	41.64				✓
137398	11:35:36.81	+27:56:10.5	53816_2219_442	0.0594	9.03	40.36				✓
160572	13:06:03.91	+19:48:22.5	54499_2616_630	0.0645	9.36	39.95				✓
256630	12:48:19.44	+05:42:25.8	52426_847_456	0.0818	9.34	40.38				✓
265562	23:36:01.88	-00:31:59.4	51821_384_106	0.0833	9.21	40.72				✓
278324	13:01:48.03	+01:37:18.6	52027_524_260	0.0855	9.01	41.90				✓
286382	13:19:57.21	+00:25:53.8	51984_296_471	0.0870	9.28	40.50				✓

Table A7. Mid-IR selected AGN candidates - 4/4. In the first column we list the object IDs used in this work. Stellar masses are given in solar masses M_\odot . The [O III] luminosity is given in erg/s. The last four columns show by which selection criteria the sources are classified as AGN.

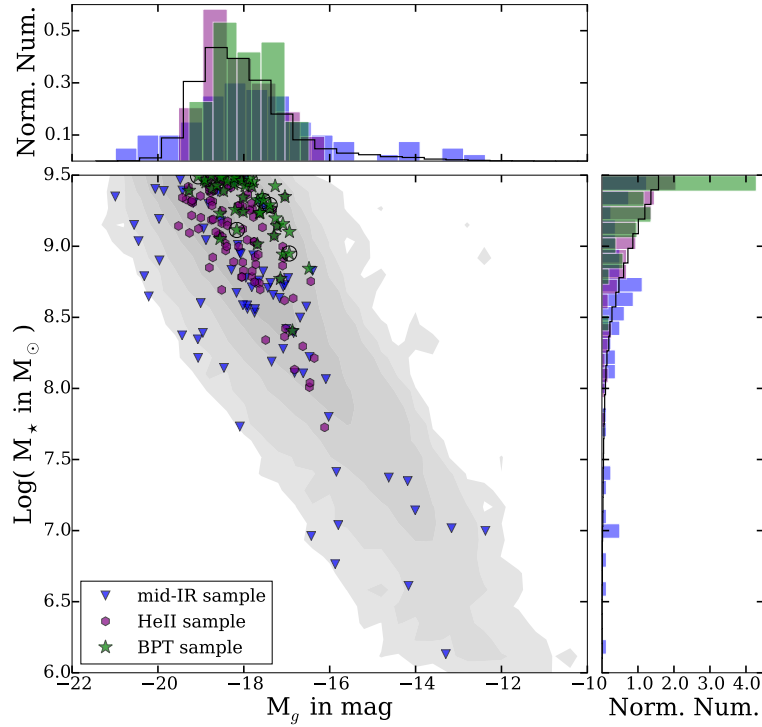


Figure B3. Same as Fig. B1 but for the mass versus absolute g -band magnitude distribution. Mid-IR selected AGN candidates are found also at lower masses and at both higher and lower g -band magnitudes compared to the optically selected candidates.